

Particle Image Velocimetry Investigation of Void Seepage through a
Simulated Ice Jam

By

Andrew Gordon Murray

A Thesis submitted to the Faculty of Graduate Studies of
The University of Manitoba

In partial fulfillment of the requirements of the degree of

MASTER OF SCIENCE

Department of Civil Engineering

University of Manitoba

Winnipeg

Copyright © 2020 by Andrew Murray

Abstract

Many rivers in cold climate regions can experience ice jams, which can be significant contributors to heavy flooding, especially when coinciding with higher spring runoff flows. Due to the danger and unpredictability inherent with ice jams, laboratory studies are often used to analyse flow conditions underneath ice jams. An experiment was conducted in the small-scale Particle Image Velocimetry (PIV) flume at the University of Manitoba, using polyethylene pellets to simulate the accumulation of ice pieces in a breakup ice jam. The goals of this experiment were to examine the flow conditions under a simulated ice jam using PIV, and develop a methodology for calculating void seepage, the portion of total river flow within the jam. Contours and profiles were presented for average velocities and turbulence statistics for three test conditions at a constant Froude number and varied upstream water depths of 5, 10, and 15 cm. Velocity profiles were integrated to calculate void seepage along the jam, with the percentage of seepage then related to the relative thickness of the ice jam. Seepage values were found to be often near 5% of total flume discharge, reaching as high as 14% at the thickest portions of the ice jam. A cubic polynomial was fitted to the dataset relating the recorded seepage ratios to the relative jam thickness. The recorded seepage flow and estimated hydraulic gradient was also used to calculate a minimum seepage velocity parameter for the model ice jam, found to be $\lambda = 0.57$ m/s.

I would like to offer sincere thanks to my academic advisor, Dr. Karen Dow, for her unwavering support and motivation throughout the course of my academic career. I would also like to thank my other committee members, Dr. Shawn Clark and Dr. Mark Tachie, for their time and efforts in the review process of this thesis.

I would also like to express appreciation to the Natural Science and Engineering Research Council of Canada and the University of Manitoba for enabling this research.

I would like to thank Dr. Ebenezer Essel, Brendan Pachal, and Alexander Wall for their expertise in creating and refining this experiment. Lastly, I must thank Parya and the rest of my friends and colleagues for ensuring my work at the University remained enjoyable and exciting while I worked toward this goal.

Table of Contents

Abstract	i
List of Tables	vi
List of Figures	vii
1 Introduction.....	1
1.1 Motivation	1
1.2 Objectives.....	2
1.3 Thesis Organization.....	3
2 Literature Review.....	5
2.1 Ice Jam Processes	5
2.1.1 Types of Ice Jams.....	5
2.1.2 Ice Jam Mechanics	7
2.2 Flow Characteristics.....	14
2.2.1 Roughness	14
2.2.2 Seepage	15
2.2.3 Velocity Distributions and Shear Stresses	18
2.2.4 Turbulence	20
2.3 Particle Image Velocimetry.....	21
2.3.1 Principles.....	21

2.3.2	Technological Requirements	23
2.3.3	Data Processing.....	25
3	Methodology	29
3.1	Experimental Setup	29
3.1.1	Model ice	29
3.1.2	Flume	31
3.1.3	PIV Setup	34
3.2	Procedures	36
3.2.1	Creation of a Jam	36
3.2.2	PIV Capture	38
3.2.3	Test Conditions	43
3.3	Data Processing	44
3.3.1	Adaptive Correlation.....	44
3.3.2	Post-processing code.....	45
3.3.3	Thickness Measurement.....	45
4	Results and Analysis	50
4.1	Flow Conditions	50
4.1.1	Overview	50
4.1.2	Average Velocities.....	51

4.1.3	Turbulence	60
4.2	Void Seepage.....	67
5	Discussion	76
5.1	Seepage.....	76
5.2	Secondary Flow	78
5.3	Limitations and Sources of Error	81
6	Conclusions and Future Work	84
6.1	Future Work	85
	References	87
	Appendices.....	93
A.1	Convergence Test.....	93
A.2	Spatial Resolution Test.....	96
A.3	Jam Profile Image Processing	98
A.4	Secondary Flow	100
A.5	Uncertainty Analysis	102
A.6	Model Ice Properties	105

List of Tables

Table 1 - List of capture planes and their locations. 40

Table 2 - Summary of design test conditions..... 44

Table 3 - Comparison of measured and calculated water depth. 49

Table 4 – Summary of recorded flow conditions..... 50

Table 5 – Bias limits for streamwise and vertical mean velocities U and V. 103

Table 6 – Precision error for streamwise and vertical velocities, U and V. 104

Table 7 - Model ice density measurements..... 105

List of Figures

Figure 1 - Forces acting on a small piece of an ice jam. (Adapted from Pariset et al. 1966)	8
Figure 2 – Representation of an ice jam profile, based on (Beltaos, 1995).	10
Figure 3 - Greyscale image of a PIV frame, captured in this experiment.	23
Figure 4 - Visual approximation of cross-correlation.	28
Figure 5 – Unpainted HDPE pellets and blocks.	29
Figure 6 - Laser sheet on unpainted HDPE pellets.	30
Figure 7 - Painted HDPE model ice pellets.	31
Figure 8 - Recirculating flume and aluminum traversing frame.	32
Figure 9 - Flume layout with capture planes.	33
Figure 10 - Nd:YAG laser used in this experiment, mounted below the flume.	35
Figure 11 - Center-alignment and calibration tool positioned in flume.	36
Figure 12 – Ruler-measured jam thickness.	42
Figure 13 – Top (red) and bottom (blue) elevations from image processing.	48
Figure 14 – Calculated ice jam thickness profiles from image processing.	49
Figure 15 - Average streamwise velocity (U , m/s) contours with streamlines	52
Figure 16 – Normalized streamwise velocities	54
Figure 17 - Average vertical velocity (V , m/s) contours	56
Figure 18 – Vertical velocity profiles normalized by U_{\max}	57
Figure 19 – Mean Shear contours (dU/dy , s^{-1}).	59
Figure 20 – Streamwise Reynolds Stress (u^2 , m^2/s^2)	61
Figure 21 – Streamwise Turbulence Intensity normalized by U_{\max}	62

Figure 22 – Wall-normal Reynolds Stress (v^2 , m^2/s^2).....	63
Figure 23 – Normalized Vertical Turbulence Intensity	64
Figure 24 – Reynolds Shear Stress (uv , m^2/s^2) contours	66
Figure 25 – Reynolds Shear stress normalized by U_{max2}	67
Figure 26 - Calculated specific discharge values along channel using equation 22.	69
Figure 27 - Corrected specific discharge values along channel.....	70
Figure 28 - Calculated Seepage Ratio along channel	72
Figure 29 - Seepage Ratio related to jam Thickness Ratio	73
Figure 30 - Fitted polynomial relating Seepage Ratio to Thickness Ratio.	75
Figure 31 - Upstream mean velocity contours for Case 15	78
Figure 32 - Upstream mean velocity contours for Case 5.	79
Figure 33 - Mean velocity profiles for U (left) and V (right)	80
Figure 34 - Estimation of secondary flow cells	81
Figure 35 – Convergence for first order mean velocity statistics.	93
Figure 36 – Convergence results for second order turbulence statistics.....	94
Figure 37 – Convergence results for third order turbulence statistics.	95
Figure 38 – Spatial resolution test results.	96
Figure 39 – Workflow diagram for image processing code.	98
Figure 40 - Difference plots for U (left) and V (right) for off-center planes	100

1 Introduction

1.1 Motivation

Rivers in cold regions are often subject to annual freeze-up and break-up processes, both of which have significant effects on the flow conditions of the river. Ice jams are arguably the most dramatic of these effects, as pieces of floating ice can pile up against one another, constricting the cross-sectional area available for water flow as well as increasing the flow resistance caused by the roughness of the jam. This reduction in channel conveyance can lead to rises in upstream water levels many times greater than what occurs with a smooth, competent ice cover, and an ice jam can form suddenly enough to cause this flooding effect quickly. In addition to their impact on flood levels, ice jams can also cause damage to riverfront property due to the presence of large ice floes and rubble piles. For these reasons ice jams are a significant risk factor to be considered by hydraulic engineers in any cold-climate project, and understanding their formation and behaviors is important for confidence in the safety of lives and property affected by ice jam flooding.

Flow conditions under an ice jam are complex and difficult to study due to the unpredictability of jams, and the safety hazards associated with field measurements of ice jam features. Knowledge gaps remain in understanding behaviours such as ice floe mechanics and the flow velocities that occur underneath the jam. These factors are important to study for developing realistic ice jam models for simulating or predicting a jam's effects on river hydraulics.

One concern of hydraulic models is creating an accurate representation of the flow conditions that would occur in the field. For ice jam modelling this includes not only understanding of the

bulk discharges under a jam, but also features such as the shear stresses and turbulence that occur under the jam, as these exert additional forces which could alter the development of the jam. These are difficult to study in field jams but have been examined in several laboratory studies with simulated ice jams (Nyantekyi-Kwakye, et al., 2018; Healy & Hicks, 2006). Improving on this with more precise measurement techniques and closer-to-realistic simulated jams is important to ensure hydraulic models can be validated against realistic conditions.

Another knowledge gap exists in the measurement of flow through an ice jam, known as void seepage, where a portion of the river discharge moves between the ice floes composing an ice jam. This is a factor that has been difficult to study beyond conditions where the jam is *grounded*, or thick enough to reach the channel bed, as this condition means that all flow must go through the jam and seepage can simply be measured by knowing the total river flow (Wong, et al., 1985; Beltaos, 1999). However, seepage still occurs when a jam is floating, and quantification of this flow would be important for validating and improving the accuracy of ice jam hydraulic models.

1.2 Objectives

This study aims to expand on past work by Nyantekyi-Kwakye et al. (2018), which used Particle Image Velocimetry (PIV) techniques to study the flow conditions under an acrylic ice jam geometry. The investigation here will focus on a laboratory ice jam made of discrete floating model ice pieces, rather than constructed ice jam geometries used in previous PIV-based studies.

Use of a floating model ice jam allows flow to pass through the jam rather than only under it, so this research also proposes a method for direct measurement of seepage flow using integration of

the velocities acquired through PIV. Past measurements of seepage have only been possible with fully grounded jams, however, use of PIV will improve on these methods by allowing measurements under a floating jam without any equipment disturbing the flow or the jam. The seepage measurement technique studied in this thesis would be the first method for study on floating ice jams.

The research objectives are as follows:

- Analyze the velocity, mean shear stress, and turbulence characteristics of water flow under a model ice jam, using particle image velocimetry.
- Develop a methodology for quantifying seepage flow through non-grounded model ice jams through integration of the mean velocity profiles underneath it.
- Examine the relationship between seepage flow and the thickness of the ice jam.
- Determine the changing significance of seepage flow as the open flow area is decreased.

1.3 Thesis Organization

The following section of this thesis contains a literature review on the current knowledge on both ice jam formation and analysis, as well as past research on seepage flow through ice jams, followed by the principles of particle image velocimetry.

The methodology, Chapter 3, describes the experimental setup and test conditions, along with the specific settings used for the PIV analysis.

Results and Analysis, Chapter 4, includes all contours and select profiles plots for velocity and turbulent statistics studied in this project, for each test case. This section also describes the process required for calculating seepage flow from PIV velocity data.

Following this, a discussion section presents the challenges and sources of error for this project, as well as the limits of the experimental design and potential resolutions. Potential future work is also described.

2 Literature Review

2.1 Ice Jam Processes

Ice jamming will typically occur during either the freeze-up period in early winter or during breakup in spring, or during a historically less common mid-winter thaw which may cause an ice jam that can re-freeze until breakup. Jams can be comprised of a mixture of floating solid ice floes, ice slush, or ice pans, with breakup jams mostly comprised of the former and freeze-up jams primarily comprising the latter. These ice pieces reach a point in the river at which their motion is stopped, generally by a channel obstruction caused by bridges or width constrictions which may allow blocks of ice to “bridge” the width of the channel in a stable way, or by a sudden reduction in flow velocity caused by increased channel depth or an estuary as it enters a large water body. (Ashton, 1978)

2.1.1 Types of Ice Jams

Depending on the conditions during their formation, an ice jam can develop as a *surface jam* or a *thickened jam*. Surface jams rarely pose risk for flooding or infrastructure damage, while thickened jams can restrict flow significantly more and are therefore the more commonly researched variety. These jams are characterized as *narrow* or *wide channel* jams (Pariset, et al., 1966) where thickness is dependant on the ability for the jam to transfer forces to the river banks, or as *hanging dams*, formed by the continuing deposition of ice under a stable ice cover. Each of these thickened jams come with potential for infrastructure damage or flooding since under the right conditions they can develop to obstruct a large portion of a river’s cross section. Reduction

in cross-sectional area available to flow combined with the addition of a rough surface boundary made by the ice jam both contribute to an increase in upstream water level.

Frazil ice commonly forms during the freeze-up period when turbulent water becomes supercooled and consists of many suspended small discs up to 5 mm in size (Ashton, 1978) which accumulate into slush and larger pans. Since frazil ice tends to form in open water sections of a river where the water can lose heat to the atmosphere more quickly, it will often be carried to a downstream location where an intact cover is present, at which point it will float against either the underside or upstream edge of the cover and come to rest. Freeze-up ice jams can form when pans accumulate and thicken through consolidation, as described in section 2.1.2.

Alternatively *hanging dams* are a result of this accumulation under the ice cover rather than upstream of it, and they can continue to grow to extreme thicknesses if the supply of new frazil ice continues (Beltaos, 2008).

Jams during breakup are often more sudden and severe than those during freeze-up, being capable of forcing high flood levels upstream at very short notice. These breakup jams often have greater flooding potential than at freeze-up, since they often coincide with increases in runoff from snowmelt (Beltaos, 2008). During the spring thaw, the strength or *resistive force* of an ice cover will decrease as warmer air and water temperatures begin melting the top and bottom of the cover. Similarly, spring runoff tends to result in a significant increase in flows which in turn increases water velocity and depth, causing greater shear and bending forces to be applied to the cover. At some point the combination of decreasing strength and increased applied force will reach a point to cause the cover to break. *Thermal breakup* occurs in the case where the ice primarily melts in place with little increases in fluid shear stress, while a *dynamic*

breakup occurs primarily due to hydraulic forces dislodging an ice cover which still retains most of its winter strength and involves a greater jam potential (Beltaos & Burrell, 2006).

Breakup jams tend to contain much larger individual blocks than those created by frazil slush or pans, which when piled together form a jam where roughness tends to increase with jam thickness. (Beltaos, 2001). Flow must travel around the large ice floes as they protrude from the jam, which creates chaotic flow conditions which are very difficult to measure in the field. Even in a laboratory setup, equipment such as acoustic Doppler velocimeter (ADV) probes are intrusive or could be damaged by ice pieces.

2.1.2 Ice Jam Mechanics

Regardless of their season of occurrence, an ice jam can be analyzed in a similar fashion through force balances acting on the ice rubble. Based on knowledge of the evolution of lumber jams against booms near lumber mills, (Kennedy, 1958) ice jams were considered to behave similarly, by thickening to the point where the internal strength of the jam is equal to those applied by shear stresses applied by flowing water. At the upstream side the jam will have a small thickness, while proceeding downstream will eventually accumulate enough stress that it will cause *shoving* which causes the downstream ice to thicken into additional layers, as demonstrated by Zufelt & Ettema (1997). Pariset et. al (1966) added the classification of *narrow* and *wide channel* jams, where a narrow jam possesses the internal strength to transfer all applied shear stresses directly to the banks of the river and any increase in thickness is dependant on hydraulic conditions at the leading edge. A wide channel is not strong enough and therefore collapses, thickening until such a point that it gains the required internal strength. Most research into ice jams, including that

done in this thesis, has been on wide channel jams as they are the most common to occur in the field.

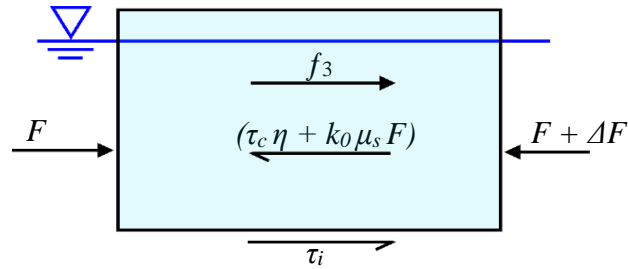


Figure 1 - Forces acting on a small piece of an ice jam. (Adapted from Pariset et al. 1966)

Calculation of the forces acting on these jams is based on a force balance upon a thin cross section of the jam. One such force balance (Pariset, et al., 1966) is shown in Figure 1, from which the following expression for the force per unit width in the jam can be derived. Equation 1 below describes the force per unit width acting on the jam at any given distance downstream of the leading edge. It can be expected that, as the shear stress applied by water τ_i , acts along the entire underside of the jam, the effects of this stress will continue to build up with increasing distance from the upstream end as the jam must resist not only the forces acting at that location, but also the cumulative forces pushing against it from upstream. These are resisted by cohesion and friction at the channel banks, shown by the force in brackets. If these resistive forces are less than the accumulated driving forces, the jam would collapse at that location, causing it to thicken until such a point where these forces are balanced.

$$F = \frac{B}{2k_0\mu_s}(\tau_i + f_3) - \frac{\tau_c t_i}{k_0\mu_s} - \left[\frac{B}{2k_0\mu_s}(\tau_i + f_3) - \frac{\tau_c t_i}{k_0\mu_s} - f_1 \right] e^{\left(\frac{-2k_0\mu_s x}{B}\right)} \quad 1$$

F = longitudinal force acting in the ice jam

x = distance from upstream end of the jam

B = width of the jam

k_0 = coefficient of lateral thrust

μ_s = coefficient of static friction between ice and the river bank

τ_i = viscous shear stress acting on the underside of the jam

τ_c = cohesive stress of the ice at the bank

t_i = jam thickness

f_1 = force exerted by flow on the upstream end of the jam

f_3 = downstream component of the weight of the ice cover = $\rho_i g t_i S$

S = slope

g = gravitational acceleration

ρ_i = density of ice

From equation 1 comes the definitions for the previously mentioned *narrow* and *wide channel* jams. If the term in square brackets is positive, the resulting F will increase with increasing x , representing a *wide* jam where the internal forces continue to accumulate down the jam. If the term in square brackets is negative, the resulting F is largest when $x = 0$, representing a *narrow* jam where the accumulating forces are fully counteracted by resistance at the banks, and the ice jam progression is dependant only the hydraulic conditions at the leading edge. (Pariset, et al., 1966)

Beltaos (1995) describes the shape of a thickened ice jam and classifies the wide jam's profile into several regions, as shown in Figure 2. The "downstream transition" region that first builds up against an intact cover or obstruction is also known as the "toe" of the jam, growing to the greatest thickness and having the largest impact on upstream flood levels. The thickness of the

ice jam decreases both upstream where the gathered shear stresses decreases and therefore requires less internal strength to resist, and downstream where the supply of ice is less, and blocks can be entrained and carried away. Upstream of the toe can exist an “equilibrium” section of constant thickness, which forms if the jam is long enough to reach a point where the thickness and flow conditions are uniform. The equilibrium section may not actually develop in a jam depending if there is a sufficient supply of incoming ice for a sufficient amount of time to reach uniform conditions.

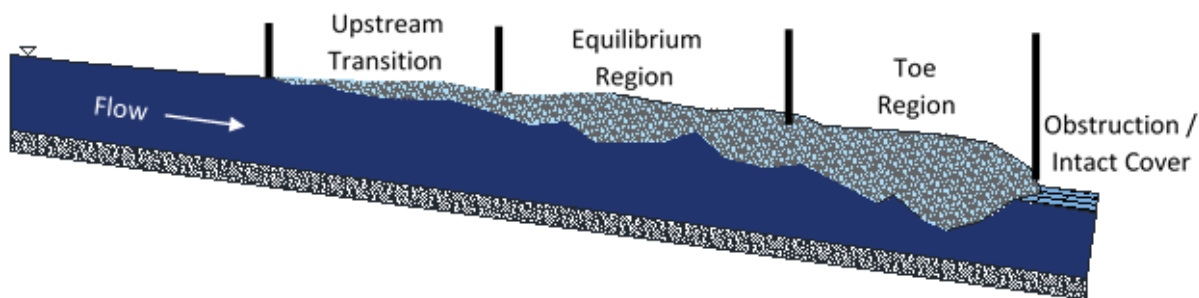


Figure 2 – Representation of an ice jam profile, based on (Beltaos, 1995).

The thickening process of ice jams has been studied in a range of laboratory conditions using model ice, usually made of high-density polyethylene (HDPE) or a similar floating plastic. Model ice jams can be developed by floating this material in a flume at whatever flow conditions are intended to be studied Zufelt & Ettema (1997). qualitatively demonstrated the thickening process of a model ice jam using both real ice pieces and small polyethylene cylinders, where the ice was allowed to collect against a screen in a single layer at low flow rates, after which the flows were increased until the surface jam strength was exceeded and shoving began. They observed the progression of a *shoving front* from upstream to downstream, which would eventually reach the screen and thicken until reaching its needed internal strength. The newly

thickened and immobile section would grow upstream and was called the *stopping front*. (Zufelt & Ettema, 1997) They also conducted a set of experiments to compare the thickness of the model jams after thickening to what could be expected by equilibrium thickness calculation, finding that the mode of jam failure could cause jams to reach a range of thicknesses, some of which can be larger than that of an equilibrium calculation.

Model ice jams of floating plastic have been utilized by several other researchers (Healy & Hicks, 2006; Wang, et al., 2016; Wang, et al., 2012; Wong, et al., 1985; Ettema & Muste, 2001; Ettema, 2017) to examine the development of ice jams in a variety of flow conditions.

Polypropylene pellets similar to those used in this thesis have in the past been used to show the behaviours of jams accumulating around bends (Ettema, 2017; Urroz & Ettema, 1992) and channel confluences (Ettema & Muste, 2001) by constructing flumes with these shapes, manually discharging the plastic beads at the upstream end, and allowing them to jam against a mesh screen. Healy & Hicks (2006, 2007) created model ice jams using HDPE squares floated against a plywood model intact cover. In a large, 32 m long flume at the University of Alberta, they were able to allow thick ice accumulations to form naturally without outside intervention. The flow underneath these jams was measured with a vertical array of Prandtl tubes at two locations along the jam, providing good representation of the velocities under the jam (Healy & Hicks, 2006) as well as how the thickness of the jam reacts to changes in channel discharge (Healy & Hicks, 2007).

In addition to the wide channel jam approach of considering the jam as a granular material with consistent material properties, later researchers (Coutermarsh & McGilvary, 1994; Dow Ambtman, et al., 2011) analyzed ice floes individually with the goal of understanding the

physical processes acting on a single unit of ice. This knowledge could then be applied to many individual blocks to more accurately model a complete ice jam with closer to true physical representation. These analyses tend to focus on predicting what circumstances will cause an individual block to either come to rest as part of a jam or become entrained in the flow and carried downstream beneath the jam. An ice floe's behavior is dependent on several factors including the shape, thickness, and density of a floe, as well as flow velocities underneath and around the block. First described was the “no-spill” condition where an ice floe is assumed to become unstable once the leading edge rotates downward enough to become submerged (Pariset & Hausser, 1961). After this point water spilling over the top of the block is assumed to continue pushing the block to overturn.

Uzuner & Kennedy (1972) and Ashton (1974) developed overturning criteria based on empirical relationships relating the static forces exerted on a block to block geometry such as thickness and density. Equation 2 (Ashton, 1974) finds the critical incoming water velocity v_c which would cause overturning, based on block thickness, where t_i is block thickness, H is upstream water depth, and g is gravitational acceleration. Theoretically this equation could be solved for blocks of varied thickness to determine the water velocities which would cause them to entrain in the flow. The left-hand-side of equation 2 is known as a critical Froude criterion for submergence, where the densimetric Froude number is calculated with a characteristic length of t_i . The choice of characteristic length is somewhat arbitrary and can also be represented with respect to H instead of t_i .

$$\frac{v_c}{[gt_i(1-s_i)]^{1/2}} = \frac{2\left(1-\frac{t_i}{H}\right)}{\left[5-3\left(1-\frac{t_i}{H}\right)^2\right]^{1/2}} \quad 2$$

Contrasting the critical Froude criterion described in equation 2, later research attempted to move away from empirically based solutions to a physical model based on static force balances acting on blocks. Daly and Axelson (1990) derived equations to determine the righting moment acting upon a block as it begins rotating downward, with the expectation that a block will overturn once the downward overturning pressures are larger than the peak righting moment. This research contradicted the “no-spill” condition assumed in previous research, finding instead that the peak righting moment was dependant on several factors including block length, which had previously been considered insignificant.

Countermarsh and McGilvary (1994) expanded on this research by studying the forces exerted on a fixed rectangular polyethylene block by measuring the hydrodynamic pressure distribution. This avoided empirical relationships for forces acting on ice, and instead aimed to quantify the forces with direct pressure measurements. They described zones of positive stabilizing pressures and negative overturning pressures and compared these to hydrostatic righting moment caused by buoyancy, with the static stability limit being the point at which the overturning forces overcome the righting forces. They also analyzed blocks with varied length, thickness, and water depth and found both length and thickness ratios to have significant impacts on stability, despite length being ignored in previous research.

Dow Ambtman et al. (2011) used piezometric pressure taps and PIV optical measurement to expand analysis of the pressures and velocity distributions underneath and quantify the pressure effects caused by recirculation near the leading edge of a single simulated ice floe, and develop

methods for predicting stability of a single block using a static force-moment analysis. This work was expanded upon by Zhao et al. (2017), who used simulated polyethylene ice floes to examine the behavior of blocks sitting underneath an ice cover rather than at the leading edge, and used a CFD model of the same blocks to study the flow diverting around the blocks rather than under them, and estimate what effect this would have on the force-moment stability analysis of the block. While these studies are some of the most recent advancements in the field and good representations of the specific single-block conditions they study, there remains significant knowledge gaps regarding the effects of unpredictable collisions, odd-shaped blocks, and unsteady or chaotic flow, all of which would affect the development of a real ice jam.

2.2 Flow Characteristics

2.2.1 Roughness

A primary factor influencing the flow impacts of an ice jam is the roughness of the underside, measured as either absolute roughness (deviation of thickness from the jam's average thickness), or Manning coefficient. Manning roughness has been measured by Nezhikhovskiy for freeze-up jams, showing that the roughness values increase with an increase in thickness and was largest for jams comprised of large ice floes (Nezhikhovskiy, 1964). Beltaos (2001) measured the roughness of breakup jams using depth probes that could be floated along underneath a jam, recording the elevation of the underside as it rolls along. They found the absolute jam roughness to correspond well with previous Manning's n values and increased linearly with increases in thickness.

An important factor affecting the flow conditions under a jam is *relative roughness* of the jam underside compared to the bed. To study the effect of relative roughness, Pahlavan et al. (2016) constructed a solid surface boundary in a laboratory flume designed to imitate the profile of a simplified ice jam, with roughness elements attached to the surface and bed. The laboratory setup simulated equilibrium, upper toe, and lower toe regions and recorded velocity profiles at several locations in each of these regions using an ADV. Nyantekyi-Kwakye et al. (2018) expanded on this research with PIV, using smaller acrylic channel with the same study regions. The PIV results confirmed that the local maximum streamwise velocities increase in the rough case.

2.2.2 Seepage

As it is possible for an ice jam to thicken enough to occupy the full cross-section of a river, it must also be the case that flow can pass between jammed ice floes as seepage to provide an outlet for the continued river discharge. While these *grounded jams* are the most extreme example of seepage through a jam, it is still the case that flow can move through a non-grounded jam as well.

A simplified investigation on grounded ice jams was conducted by Wong et al. (1985) which simulated the effect of a grounded ice jam on upstream water levels. The researchers dropped a cage filled with rocks into a flume with constant flow to simulate the sudden creation of a grounded ice jam, then recorded the water level upstream and downstream of the cage until it approached a new steady state. This research was preliminary but showed that seepage through the simulated ice jam was dominated by turbulent flow in voids rather than laminar flow, where the velocity is proportional to the square root of hydraulic gradient (Wong, et al., 1985).

According to Bear (1972), the discharge through a medium with large voids (such as can be found in an ice jam) does not necessarily follow Darcy's law, but rather reduces to the following formula:

$$Q_p = \lambda A_j \sqrt{S_w} \quad 3$$

Where Q_p is the total seepage discharge (m^3/s), λ is the seepage velocity (m/s), A_j is the bulk flow area of the jam, and S_w is the hydraulic gradient. Based on this equation, discharge could be calculated by knowing only the seepage velocity and water surface profile of the jam. Bear also describes a model for determining seepage velocity as:

$$\lambda = \sqrt{k \frac{p^3}{1-p} g d_s} \quad 4$$

Where k is a dimensionless coefficient generally considered to be 0.7 for ice (Wong, et al., 1985), p is the porosity of the rubble commonly taken as 0.4 (Prowse, 1990), and d_s is related to rubble size according to the following equation:

$$d_s = \frac{6t_i}{2 + \frac{Pt_i}{A_b}} \quad 5$$

Where t_i is the ice thickness, P is the perimeter of the block, and A_b is its area. Obviously in the field such exact measurements for block sizes is unknown and varies greatly, however d_s and p , and k can all be estimated with rule-of-thumb values.

With these equations for seepage velocity, the calculated flow rate is at best still dependent on at least one entirely empirical parameter (k) even in a best-case scenario where an engineer has access to detailed measurements of ice floe geometries and porosity. For this reason, many studies aim to simply measure and report the seepage coefficient λ directly rather than the

dimensionless coefficient k . Beltaos (1998) published a field study measuring the flow through voids in breakup jams on the Credit River in Ontario. The measurements were taken in two years when favorable conditions caused midwinter breakups which jammed against a water control structure, causing a grounded ice jam to form and remain intact. Using measured river flow and water surface profiles, seepage velocities were calculated ranging from $\lambda = 1.6$ to 2.1 m/s.

Arthur (2012) performed a laboratory study on the laminar flow properties through and over a porous medium using PIV. They constructed several simulated porous media by using grids of rods spaced to emulate a range of porosities (0.51 to 0.97) and configurations set at the bottom of the flume and extending upward partially into the flow. Velocity fields were obtained using particle image velocimetry and pressure measurements made using electronic transducers at several locations along the channel. Although this study was not dealing directly with ice, it looked at flow conditions where the porous media only occupied as little as 0.34 times the flow depth, providing a similar (but inverted) scenario to the interface between water and a porous ice jam and allowing the researchers to look at the interaction between the flow above and within the matrix. The research showed that when flowing only through the porous media, the friction factor predictably increased with lower porosities, as well as depending on the orientation of the posts (vertical, horizontal, or both), but was not significantly impacted by the shape of the rods (square or round). When flowing over top of the porous media, the same decrease in porosity increased the free flow portion from 40% to 98% and decreased penetration of fluid into the media by half and reducing the filling fraction (amount of flow area taken by the medium) from 0.75 to 0.34 caused an 18% increase in the portion of free flow (Arthur, 2012).

2.2.3 Velocity Distributions and Shear Stresses

The shear stress applied to the underside of an ice jam is the most significant component involved in forcing an ice jam to thicken, as well as potentially break and move downstream. To better predict the behavior of an ice jam, it is therefore important to more accurately quantify what magnitudes of shear stress can be expected along the entirety of the jam. Average shear stresses on a boundary are calculated as a function of the water velocity gradient near the boundary, and therefore require knowledge of the velocity distribution under the jam to estimate these values according to equation 6, where τ_l is the viscous shear stress, μ is the dynamic viscosity of the fluid, and $\frac{dU}{dy}$ is the velocity gradient.

$$\tau_l = \mu \frac{dU}{dy} \quad 6$$

Often the velocity distributions in an open channel are approximated with what is known as the *law of the wall*, which relates dimensionless streamwise velocity, U^+ to dimensionless height above the bed, y^+ according to equation 7 for flow within the viscous sublayer, and equation 8 for further from the wall. These equations normalize values based on friction velocity, U_* , estimated as $U_* = \sqrt{gRS}$.

$$U^+ = y^+ \quad \text{for } y^+ < 5 \quad 7$$

$$U^+ = \frac{1}{\kappa} \ln(y^+) + A \quad \text{for } 26 < y^+ < 0.2 \frac{U_* h}{\nu} \quad 8$$

where $U^+ = U / U_*$, $y^+ = \frac{y U_*}{\nu}$, κ is the von Karman constant (often considered 0.41), and A is a constant of integration (often considered to be 5.0). This equation is often assumed valid for

estimating velocity distributions for the entire depth of flow in an open channel, although it is only strictly valid in the region near the wall (Nakagawa, et al., 1975).

Intuitively we can expect that the velocity distribution of a river with an ice cover will be different than the same river in open water conditions as the additional static boundary of the ice cover will slow the velocities near the surface, where in open water conditions the velocity tends to remain high. Peters et al. (2017) and Pahlavan (2016) have both demonstrated the location of highest velocity is moved closer to the bed after the addition of an ice cover, compared to open channel scenarios where the highest velocity is near the surface. These were both performed by recording flow conditions under simulated ice covers using an ADV probe under either a partial ice cover (Peters, et al., 2017) or a simulated plywood ice jam (Pahlavan, 2016). The roughness of the jam relative to that of the bed will also affect to what depth the peak velocities are moved (Gogus & Tatinclaux, 1981).

To estimate the shape of a velocity profile with an ice cover, a different equation would be needed which can account for the effects of changing bed and ice roughnesses. The two-parameter power law, shown in equation 9 serves this purpose, and allows for the entire velocity profile to be estimated with a single curve, rather than the multiple layers needed for the “log law” used equations 7 and 8. (Teal, et al., 1994)

$$U = K_0 \left(\frac{y}{h}\right)^{1/m_b} \left(1 - \frac{y}{h}\right)^{1/m_i} \quad 9$$

Where y is height above the bed, h is total flow depth, m_b and m_i are inverse roughness parameters for the bed and ice (where higher values imply smoother surfaces), K_0 is a constant dependant on flow rate, and U is the mean velocity calculated at a given y .

2.2.4 Turbulence

Flow in most rivers tends to be turbulent in nature and as such the classification of turbulence structures and momentum transport is an important topic in hydraulics research (Nezu & Nakagawa, 1993). The very rough underside of an ice jam creates a particularly chaotic flow scenario as water is forced to flow around irregular ice protrusions, seep through voids, and experience a significant flow contraction and expansion at the jam toe. The amount of turbulence at a point can be quantified as *turbulence intensity* which is found by the root-mean-square of the difference between instantaneous and average velocity for each component.

$$u' = \sqrt{\overline{(u - U)^2}} \quad 10$$

$$v' = \sqrt{\overline{(v - V)^2}} \quad 11$$

$$w' = \sqrt{\overline{(w - W)^2}} \quad 12$$

Where u' , v' , and w' , are the three components of turbulence intensity in the x , y , and z directions respectively, u , v , and w , are recorded instantaneous velocities, and U , V , and W , are the time averaged velocities over the recording period all as components in their respective directions. Generally, x refers to the streamwise direction, y to the vertical direction, and z to the lateral direction. Nakagawa et al. (1975) developed empirical relationships for estimating the three components of turbulence intensity in open channel flow:

$$\frac{u'}{U_*} = 2.30e^{\frac{-y}{h}} \quad 13$$

$$\frac{v'}{U_*} = 1.27e^{\frac{-y}{h}} \quad 14$$

$$\frac{w'}{U_*} = 1.63e^{\frac{-y}{h}} \quad 15$$

where U_* is the friction velocity and y/h is the proportional height above the channel bed (Nakagawa, et al., 1975). These equations however are only useable in an open channel with a smooth bed. As an ice jam satisfies neither of these conditions, such simplified equations are not suitable for predicting turbulence under an ice jam.

It can be expected that when adding the effects of turbulent fluctuations in the flow, the actual shear stresses experienced by the fluid will differ from the laminar shear formula in equation 6. The total stress can be determined by adding a turbulent shear component as shown in equation 16, where τ is the total shear stress and $\rho\overline{uv}$ is the *Reynolds shear stress*.

$$\tau = \mu \frac{du}{dy} - \rho\overline{uv} \quad 16$$

2.3 Particle Image Velocimetry

2.3.1 Principles

Past research in the hydraulics and river ice fields, as well as most fluid flow research before PIV became more widely available requiring the measurement of flow velocities, have often utilized devices such as an ADV which require probes placed in the fluid at a single measurement point. These are limited both in recording small volumes at a time as well as being intrusive in the flow, making it difficult to measure near walls and impossible to capture turbulent structures that

would be affected by the presence of a probe. Particle Image Velocimetry (PIV) has recently become more widely used (Dow Ambtman, et al., 2011; Nyantekyi-Kwakye, et al., 2018) as it removes these disadvantages, being both *nonintrusive* to allow application in high speed flows and boundary layers as well as being a *whole field* technique collecting quantitative velocity data in a large area instantaneously rather than a single point, allowing for capture of turbulent structures and unsteady flow fields (Raffel, et al., 1998). Nyantekyi-Kwakye, et al. (2018) performed a PIV analysis most closely related to the work performed in this thesis, constructing an acrylic simulated ice jam geometry set in a flume to study the flow conditions as water moves underneath the jam. They compared the effects of both a rough and smooth jam and bed, showing how these roughness combinations affected the velocity and turbulence intensity profiles, as well as the effect on the location of their peak values.

PIV requires illuminating small tracer particles entrained in the flow and photographing them in a series of image pairs. An example of one such image can be seen in Figure 3. These image pairs can be analyzed to determine what direction the particles are moving within each of a grid of *interrogation zones*, and after post-processing each of these zones will provide a single velocity vector. In total each image pair will result in an instantaneous field of velocity vectors covering the entire image window without causing any disruption to flow. This method provides direct information on the two fundamental components of velocity, distance (how far particles move) and time (capture rate of the images), which provides better robustness compared to methods such as acoustic Doppler velocimetry which measures response time and must translate this to a velocity by relating to the speed of sound in the fluid (Adrian & Westernweel, 2011).

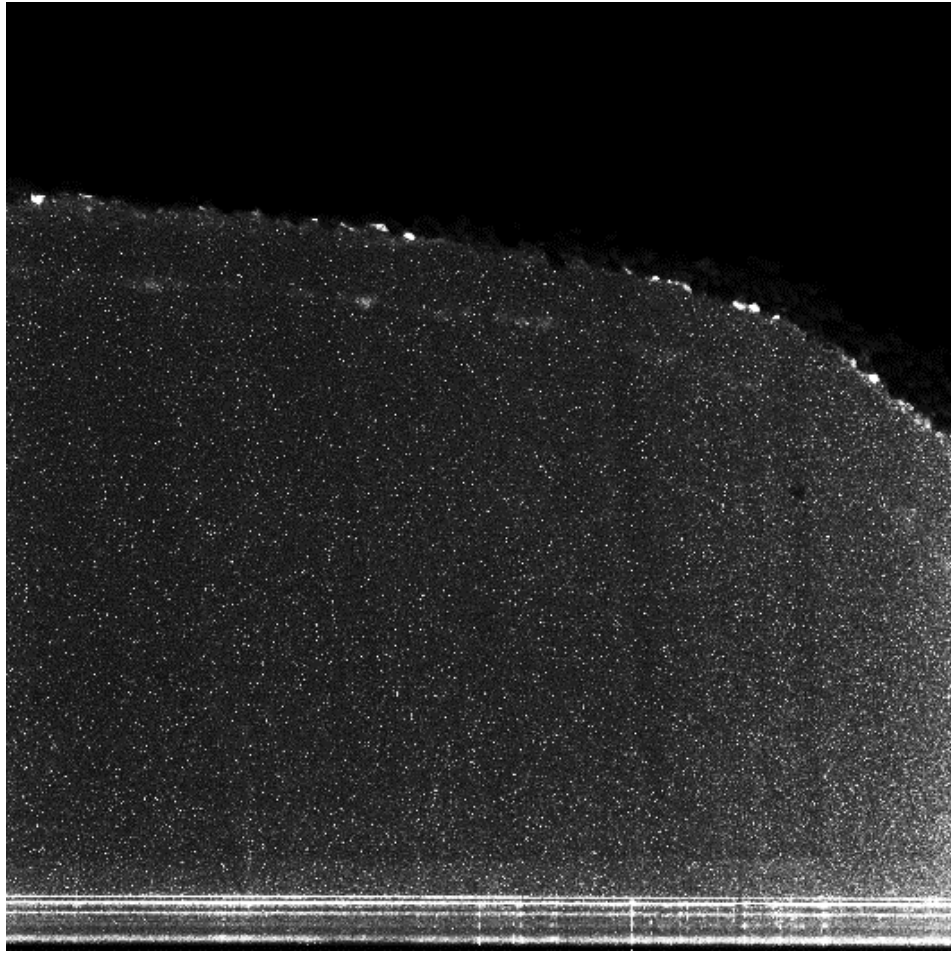


Figure 3 - Greyscale image of a PIV frame, captured in this experiment.

2.3.2 Technological Requirements

Most PIV systems will require shaping a laser into a thin illumination sheet and directed into the flow, pulsing it twice in rapid succession with a synchronized camera of high enough speed and resolution. To capture a 2D plane of 3 component velocity vectors (2D-3C), at least two cameras are used for stereoscopic imaging, and more cameras can be used to capture a volume of 3D-3C vectors.

A tracer particle and particle density must also be chosen that will most accurately reconstruct the fluid flow. A seeding particle may experience *slip* with respect to the flow, where the particle velocity will be different than the local flow velocity to provide the drag force needed to accelerate the particle (Adrian & Westernweel, 2011). Turbulent eddies can involve enormous accelerations as large as $10^5 g$, and as a result, large particles may experience a significant slip velocity, being too heavy to follow fluid acceleration as accurately. The significance of slip can be shown through the *slip velocity*, calculated based on equation 17, where U_g is slip velocity in m/s, d_p is the particle diameter, ρ_p and ρ are the densities of the particles and fluid respectively, μ is dynamic viscosity, and g is the gravitational acceleration.

$$U_g = \frac{d_p^2(\rho_p - \rho)g}{18\mu} \quad 17$$

A result of a particle's slip velocity is that it will take an amount of time to alter its own velocity when subjected to acceleration of the fluid. This timing is known as the *relaxation time* and can be calculated with equation 18 (Raffel, et al., 1998).

$$t_r = \frac{\rho_p d_p^2}{18\mu_f} \quad 18$$

Particles too small may not reflect enough light to be reliably interpreted by the camera, and it is possible for a small increase in particle size to greatly increase the amount of light scattering and image exposure. Additionally, the size at which particles appear within the captured images can affect the quality of data, as the positioning of a particle in the image space is limited to a discrete grid of pixels. This means particles smaller than one pixel will still appear as exactly one pixel, and they will exhibit a tendency of *peak locking*, which removes the ability for a cross-

correlation process to achieve sub-pixel accuracy. Particle image diameters are recommended to be at least 2 pixels to prevent peak locking. (Raffel, et al., 1998)

The *seeding density*, or concentration of these particles, is also an important factor to be considered with too few or too many particles in the image resulting in poor data quality. A common rule-of-thumb is to add seeding particles to the flow until the point where the images show approximately 10 to 25 particles in each interrogation area (Zhang, et al., 2018). Too many particles – or particularly dirty water – can result in a ‘milky’ appearance of the fluid and result in overexposed images, as too much laser light will scatter within the water rather than pass through in a single sheet. Overexposure will reduce the contrast between bright particles and the empty space between them and cause the image processing to have trouble resolving the locations of particles. Conversely, too few particles can result in interrogation areas with few or no particles, making it impossible for a velocity vector to be resolved at that location.

DynamicStudio, the software used in this thesis, will make an estimated velocity value for these situations based on adjacent interrogation areas, but having too many of these substituted values in the dataset will result in poor data quality.

2.3.3 Data Processing

The data captured through PIV directly are only a series of image pairs and turning these into useful information requires a series of processing steps from which velocities and turbulence statistics can be extracted.

Firstly, all images are divided into a selection of interrogation zones, each of which will be analyzed individually to find the displacement vector of the particles in that zone. Deciding the size and number of these zones is an important consideration with profound impacts on the

quality of data acquired. In the DynamicStudio software, the settings most commonly changed include interrogation *area*, *overlap*, and *refinement steps*. The interrogation area is defined by a number of pixels in the x and y directions (these must be “power of 2” values such as 8, 16, 32, etc.) (Zhang, et al., 2018), where larger values result in larger zones, but consequently fewer total zones fitting in the image. Smaller interrogation areas result in a higher *spatial resolution* – how closely packed the vectors are – but requires more attention to seeding density, as a smaller area makes it much more likely for no particles to be found in the area at any given time. A larger interrogation area makes it more likely that particles will be found in each image, but will have lower spatial resolution, which in turn can reduce accuracy. Best practice suggests the values for interrogation area sizes be decided based on a *spatial resolution test*, where one database of image pairs is analyzed multiple times, using each reasonable option for x and y sizes. The results of all these tests are compared with the interrogation area of the best results then being used for the rest of the analysis in the experiment.

The pulse timing between the two frames in a PIV capture must also be set before performing a complete test, as the images must be separated by enough time to allow the particles to move a detectable amount, but not move so much so as to leave the interrogation area entirely (Zhang, et al., 2018). A common rule-of-thumb is to set the pulse timing, Δt such that the fastest particle will move approximately $\frac{1}{4}$ the way across an interrogation area. The following equation can be used to estimate an appropriate pulse timing.

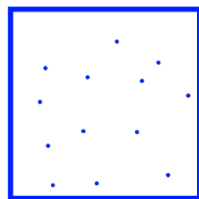
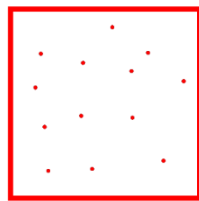
$$\Delta t = \frac{1}{4} \left(\frac{A_x(DP)(SF)}{U_{max}} \right)$$

19

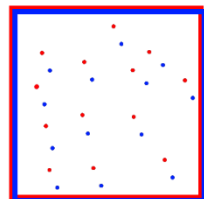
where A_x is the interrogation area width, DP is pixel pitch of the camera sensor, SF is the calibrated scale factor for the desired field of view, and U_{max} is the largest velocity found in the region.

Translating 2D image pairs into a set of displacement vectors is typically done through a process called *cross-correlation*. In this process, an interrogation zone from the first frame of an image pair is compared to the same zone in the second frame and the differences in illumination of each pixel in the zone are calculated. The first interrogation zone is then moved and the correlation is checked again, repeating the process until the best correlation is achieved, representing the displacement which makes the particles from frame 1 line up most closely with those in frame 2, represented visually in Figure 4. This cross-correlation is the industry standard method for 2D-2C PIV for its robustness, being minimally affected by image noise and changes in background illumination. The DynamicStudio formulation of cross-correlation is called *adaptive correlation*, where the cross correlation process is performed on multiple interrogation areas, starting at a larger size and repeating the process with smaller sizes in a defined number of *refinement steps*, allowing the finer vectors to be compared to coarser ones to reduce the effects of erroneous vectors (Zhang, et al., 2018).

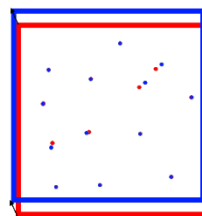
Repeating this process for every interrogation zone, in every image pair of the dataset, results in a field of instantaneous velocity vectors for every image pair. This velocity data can then be used for calculating mean velocities and turbulence statistics.



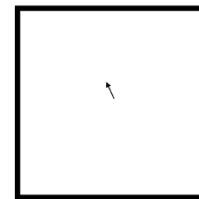
Take a small
"interrogation area"
from each image.



Overlay the
interrogation areas.



Move the second
area until the particles
align with the first.



The displacement
of the second image
shows the motion
of particles between
images.

Figure 4 - Visual approximation of cross-correlation.

3 Methodology

3.1 Experimental Setup

3.1.1 Model ice

This experiment used high-density polyethylene (HDPE) pellets as model ice floes similar to those used in experiments elsewhere (Wang, et al., 2012; Wang, et al., 2016; Zufelt & Ettema, 1997), as the small rounded shapes tend to mechanically thicken similar to rubble ice jams in a reliable manner, even at very small scales. These pellets were roughly ellipsoid shaped approximately 5 mm in size in the major axis, with specific gravity of 0.85, which is somewhat lower than that of real ice (~ 0.92). The measured porosity of the bulk, loose particles was 0.33, which is close to the often-assumed value of 0.4 for a natural ice jam.



Figure 5 – Unpainted HDPE pellets and blocks.

Geometrically the size of each pellet is approximately 2.5% the width of the channel, which would be considered on the small side when compared to the range of ice floe sizes found in field breakup jams. Preliminary tests explored the possibility of using rectangular cut HDPE model ice floes like those used by Healy & Hicks (2006, 2007), which would more closely simulate the geometry of real ice floes, including the ability for blocks to protrude into the flow. However, the PIV system used in this experiment applied a significant size constraint that was not present in Healy & Hicks' work, and it was found that these floes did not form consistent enough ice jams at the much smaller scale. Scaling down the block dimensions from that work to match the new flume would have necessitated cutting many very small (~1 cm) blocks, so it was decided to simply use the readily available pellets as they had already been known to produce reliable jams.

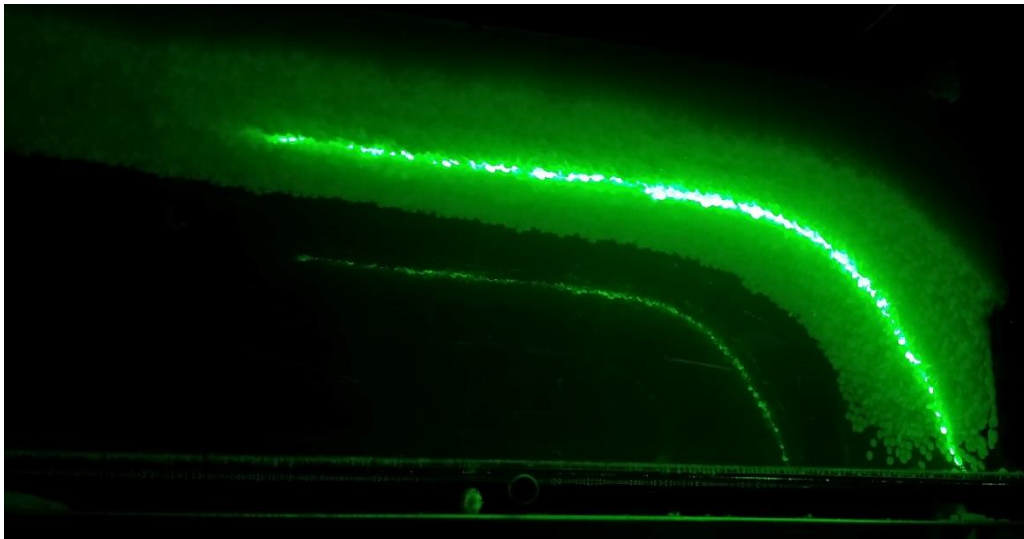


Figure 6 - Laser sheet on unpainted HDPE pellets. Reflections are visible on the flume walls.

Lastly the pellets had to be spray painted matte black for use in the PIV flume. The first attempts at PIV analysis under the ice jam resulted in significant reflection of the laser within the flume, as shown in Figure 6, overexposing the camera images near the underside of the jam as well as reflecting internally off the acrylic flume. The darkened pellets, shown in Figure 7, were stored in water when not in use to facilitate the growth of bio-film which has been shown to reduce the impact of surface tension on HDPE particles (Healy & Hicks, 2006).



Figure 7 - Painted HDPE model ice pellets.

3.1.2 Flume

The experiment was conducted in the small-scale recirculating PIV flume at the University of Manitoba, shown in Figure 8. The channel has cross sectional area of 20 cm x 20 cm, and length of 250 cm, and is equipped with a variable-frequency pump for adjustment of velocities. A 20

cm sandpaper trip was attached to the bed at the upstream end of the flume to facilitate the development of the boundary layer.

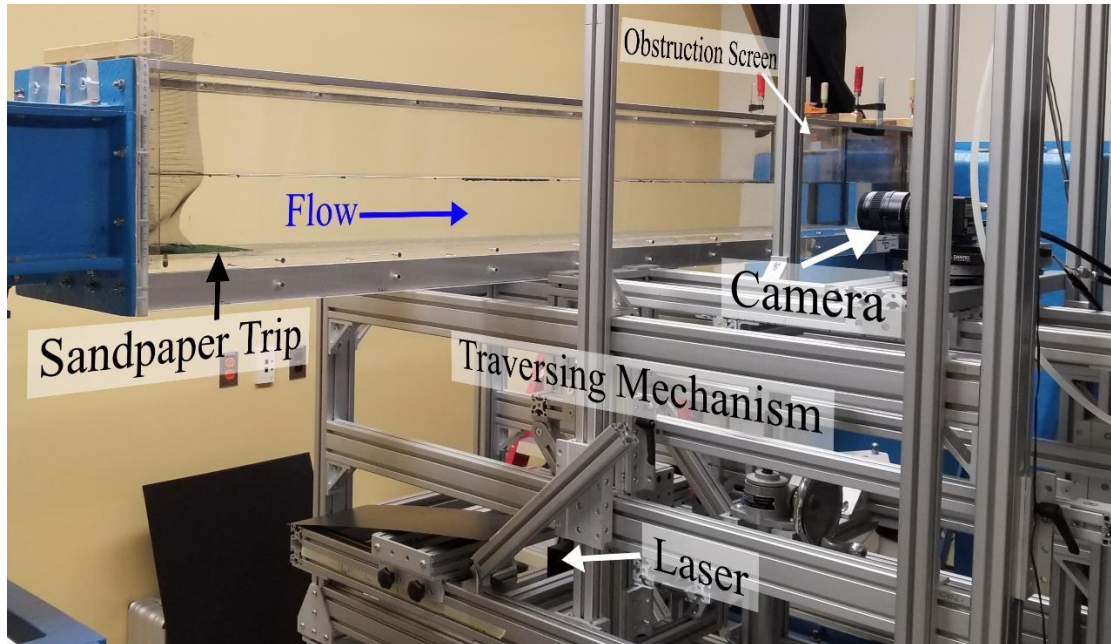


Figure 8 - Recirculating flume and aluminum traversing frame.

For forming a jam, a screen was placed in the flow to act as the toe of the jam. Similar methods have been used in other related model jams (Wong, et al., 1985) and was constructed to obstruct the flow as minimally as possible. During preliminary testing, other avenues were explored including a floating intact ice cover and a partial-depth screen, however they proved unusable in this small-scale setting. The full depth mesh screen was placed at 2120 mm downstream of the channel inlet, as shown in Figure 9. This location was chosen to be as far as reasonable from the inlet to allow the development of the boundary layer. Some distance had to be left downstream to allow for cleaning of the catch screen. A partial depth obstruction such as those used in past research (Healy & Hicks, 2006) would more closely resemble conditions that happen in the field

and would be ideal, however preliminary tests with a floating model ice cover didn't form a large enough ice jam within the confines of the small available flume area.

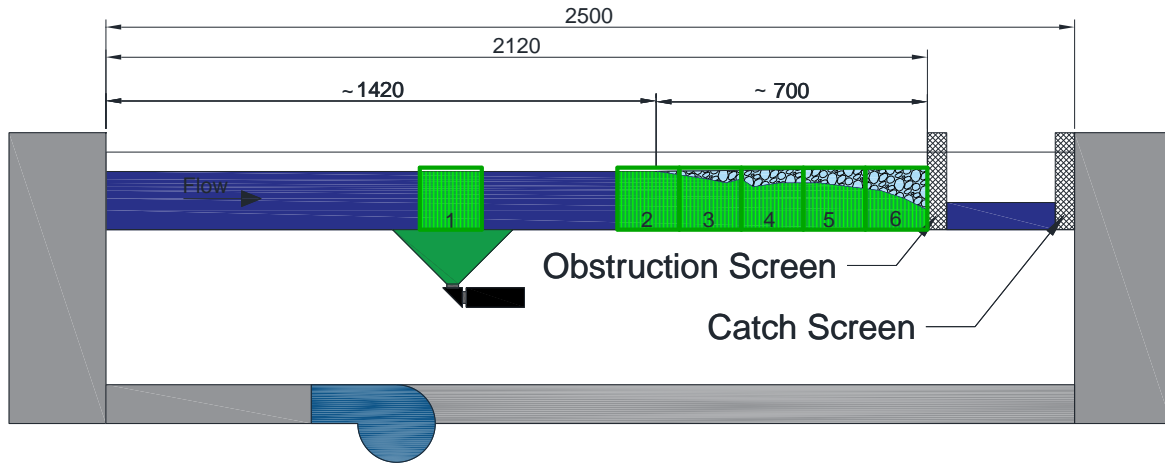


Figure 9 - Flume layout with capture planes.

A partial depth screen was also tested, which would allow some pellets to flow underneath like could happen in a real jam. However, a priority for designing this experiment was to ensure that none of the model ice particles could recirculate through the flume, as they could potentially damage the pump. A plastic mesh screen was required at the downstream end of the channel and sealed to prevent any pellets from passing, and this would collect any model ice which transported under the ice cover or screen. Over time these pellets would build up and obstruct the channel and limit the upstream velocities. Conducting the experiment with these obstructions would have required a way for continuously cleaning the catch screen, but this was not feasible to construct in this flume and will be discussed as future work.

3.1.3 PIV Setup

For this experiment, a 2D-2C planar PIV system was used. While a tomographic system was available, it was not chosen for testing as the computational effort for analyzing that 3D-3C is much higher, and this experiment would require many planes to be analyzed to capture the full length of the jam. A Nd:YAG double-pulsed laser with wavelength of 532 nm was mounted underneath the flume, as shown in Figure 10, reflected upward through a 90° planar lens. The laser had to be under the flume and upward firing to illuminate under an opaque ice cover, however, this also required the bed to remain clear, smooth acrylic and the experiment could not be tested with a rough bed insert. For the bulk of this experiment, the laser was aligned to the centerline of the flume using the device shown in Figure 11. The laser was moved off-centre by 20 mm and 54 mm after the primary experiment was completed to examine the effect of secondary circulation.

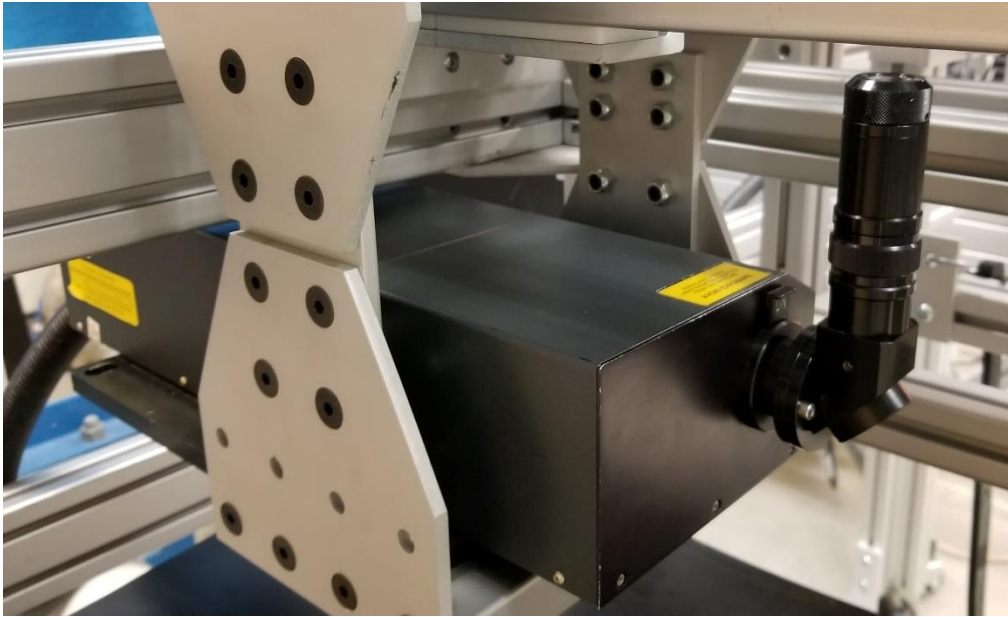


Figure 10 - Nd:YAG laser used in this experiment, mounted below the flume.

The seeding particles used in the experiment were $10\text{ }\mu\text{m}$ silver-coated hollow glass spheres, with a specific gravity of 1.4. The slip velocity – calculated with equation 19 – was $2.17 \times 10^{-5}\text{ m/s}$, which is insignificant compared to the streamwise velocities in the experiment. Similarly the calculated relaxation time according to equation 20 was $7.7\text{ }\mu\text{s}$, which is negligible compared to the pulse timing of the image pairs and therefore it is expected these tracer particles will follow the flow faithfully.

A single CCD (charge-coupled device) camera was used for image capture. The HiSense camera has a resolution of 2048×2048 pixels with pixel pitch of $7.5\text{ }\mu\text{m}$. The monochrome camera was fitted with a green band-pass filter to prevent any ambient light contamination. The camera was moved away from the flume until having a field of view of 162.3 mm , as the largest water depth expected in the experiment was 150 mm and this would ensure the entire depth can be captured

in a single plane. The same tool shown in Figure 11 was used for focusing the camera and scaling the image.

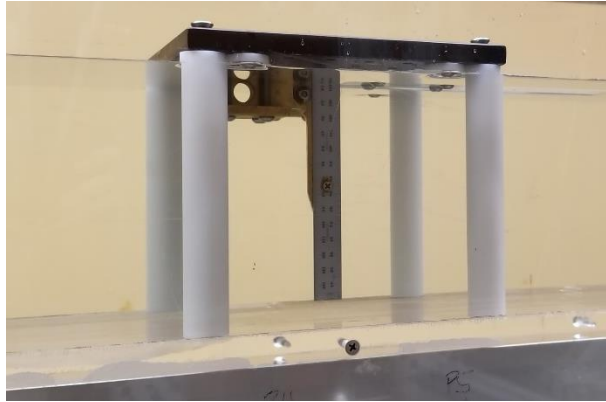


Figure 11 - Center-alignment and calibration tool positioned in flume.

3.2 Procedures

3.2.1 Creation of a Jam

Ice jams were created by manually discharging a consistent volume of model ice pellets at the upstream end of the flume and allowing them to float up against the mesh screen. Past research has shown use of both manual (Ettema, 2017) and automated (Tatinclaux & Lee, 1978) ice discharge methods; however, construction of an automated system would have again been impractical at the small flume scale. The manual ice discharge was performed as consistently as possible, distributing pellets evenly across the width of the flume with each test timed to take approximately 10 minutes to discharge the full volume of pellets, as well as waiting approximately 10 minutes to allow the jam to reach a stable state with minimal continued ice transport.

At the velocities tested in this experiment, the equilibrium thickness of the resulting ice jam generally appeared to be around 10 mm, after which the jam would simply continue to extend upstream as more pellets were added. Because this experiment was concerned with the effect of jam thickness on seepage, a very small and constant equilibrium thickness would not have been useful for most analysis. The jam therefore had to be thickened beyond what would have naturally formed at that flow velocity, which was done manually by compressing the leading edge of the jam to add additional stress and force the entire jam to thicken further. This also had the benefit of shrinking the length of the jam, which would otherwise have filled up the short upstream length of flume. The jams were thickened until they resembled an idealized jam toe, increasing in thickness relatively linearly from no thickness at the leading edge to between 3 and 50 mm near the screen. While an ideal scenario would have involved the jam thickening to these sizes naturally without outside interference, that was not possible within the constraints of this flume. It was decided that a thicker ice jam would be better for analysis even if it required manual thickening, as the experimental objectives were to study seepage through a model ice jam in whatever stable condition it exists, not to observe the actual development of the jam in a certain flow velocity.

As the pellets would come to rest against the screen, many of them would transport under the newly formed jam, and eventually settle near the bottom of the screen, restricting flow and raising the upstream water level. In most cases this would be a realistic situation, however in this recirculating flume the increase in water level caused an increase in the head difference between the upstream and downstream ends of the flume. The equipped pump was not capable of

delivering the same discharge at the new required head, and therefore increasing restriction at the screen would cause a decrease in total discharge, which would not happen in the field.

To combat this effect, the initial condition's pump frequency (and corresponding water velocity) was set higher than the desired test velocity, such that when the screen became obstructed and lowered the discharge, the final velocities would be as close as possible to desired. The required pump frequencies for each of the three test conditions was found through trial and error, and ice jams were removed and remade any time the transported pellets cause too much flow restriction at the screen. As a rule-of-thumb, if at least approximately 20 mm of the bottom of the screen was clear of transported pellets, the test could be attempted. If more of the screen was blocked, or the preliminary PIV capture showed very different velocities than expected, the jam would be removed and re-formed until the desired velocities were achieved. Resulting tests had as consistent of velocities as possible, confirmed by checking the velocities of a small PIV test and examining the peak velocities in the open water section.

3.2.2 PIV Capture

Before capturing useable PIV data, every test required a short process to ensure the data quality was maintained. Prior to making an ice jam, the pumps were run at a high frequency to stir up seeding particles that settle in the tanks and pipe, and the acrylic floor inlay was lifted and cleaned to ensure no particles or bubbles were present, which may scatter the laser as it passes through the bed. The flume walls would also be cleaned in case seeding particles or bubbles might obstruct the camera view. Once this was done, the ice jam could be formed and left until it reached a steady, stable state.

When the jam was formed and stable, PIV data was captured with the following procedure. Firstly, a short 100 image test was captured. Samples of these images were looked at for checking consistency in seeding density between planes, as well as to look for anomalies that may hamper data such as reflections or overexposure. The images were then processed through the adaptive correlation in DynamicStudio (explained in further detail in Section 3.3.1) and average velocity vectors were found. A velocity profile in the middle of this image would be checked and would be considered appropriate if it had a shape and peak velocity consistent with what was expected. If a significant issue with any of these steps existed, the jam would be removed and recreated after taking steps to correct the issue until expected velocity profiles were seen.

Before taking the full 8000 image test, the peak velocity of the 100-image set was entered into the formula in equation 19 to find the most appropriate pulse timing for that velocity, so as to ensure particles do not move too far between frames to be analyzed. If the new pulse timing was very close to what was already entered in the software, it would be considered appropriate for the full capture. However, if the newly calculated pulse timing differed significantly from the previous one, the resulting pulse timing would be entered Dynamic studio and another such “quick test” would be captured, repeating the above process until converging on the correct timing.

When all these checked had been performed the real dataset could be captured. Based on the results of a convergence test (shown in Appendix A.1), 8000 images were captured per plane. Each test condition involved capturing 6 planes. The jam was always between 700 and 800 mm long, and with a field of view of 162 x 162 mm it required 5 planes to capture the entirety of the

jam, plus an additional plane far upstream for the open water condition. The planes were numbered from 1 to 6, upstream to downstream. The locations of the upstream edge of the field of view and the alignment of all planes are summarized in Table 1.

Table 1 - List of capture planes and their locations.

	Plane #	Streamwise Location [x] from Inlet (mm)	Centerline [z] Offset (mm)	Included in Test Case		
				5	10	15
Centerline Planes	1	1017	0	YES	YES	YES
	2	1297	0	YES	YES	YES
	3	1460	0	YES	YES	YES
	4	1622	0	YES	YES	YES
	5	1785	0	YES	YES	YES
	6	1947	0	YES	YES	YES
Off-Center Planes	7	1017	20	YES	NO	YES
	9	1017	54	YES	NO	YES

The planes were captured starting at Plane 1 (upstream end) then moving all the way downstream to Plane 6, then working backward from there. This was done to capture the first and last plane as close to each other as possible temporally, as past work (Murray, et al., 2019) showed that particles could settle within the time of capturing the whole jam. In that work it was noted that the data near the end of the testing was of poorer quality than the start. To prevent loss of data quality in this experiment, the bed would have to be cleaned at regular intervals to prevent the particle settlement from impacting the laser's passage through the floor, however cleaning the bed while a jam was in place was impossible without causing disturbance to the jam. The solution decided upon was to capture two planes, then remove the jam, clean the flume, and remake the jam as close as possible to the original. The new jam would have its thickness

measured with a ruler – the closeness of the jam profiles are displayed in Figure 12– and have the velocities of a 100-image capture compared to those of the previous jam to confirm that as little as possible had changed. For the 5 cm water depth test, it was found that the seeding density and particle settlement was still acceptable for 3 planes at a time rather than 2, allowing the jam to be remade only one time. Some error is inherent to this type of procedure and will be discussed in section 5.2, however, it was deemed the best way of acquiring quality velocity and turbulence data for the entire jam.

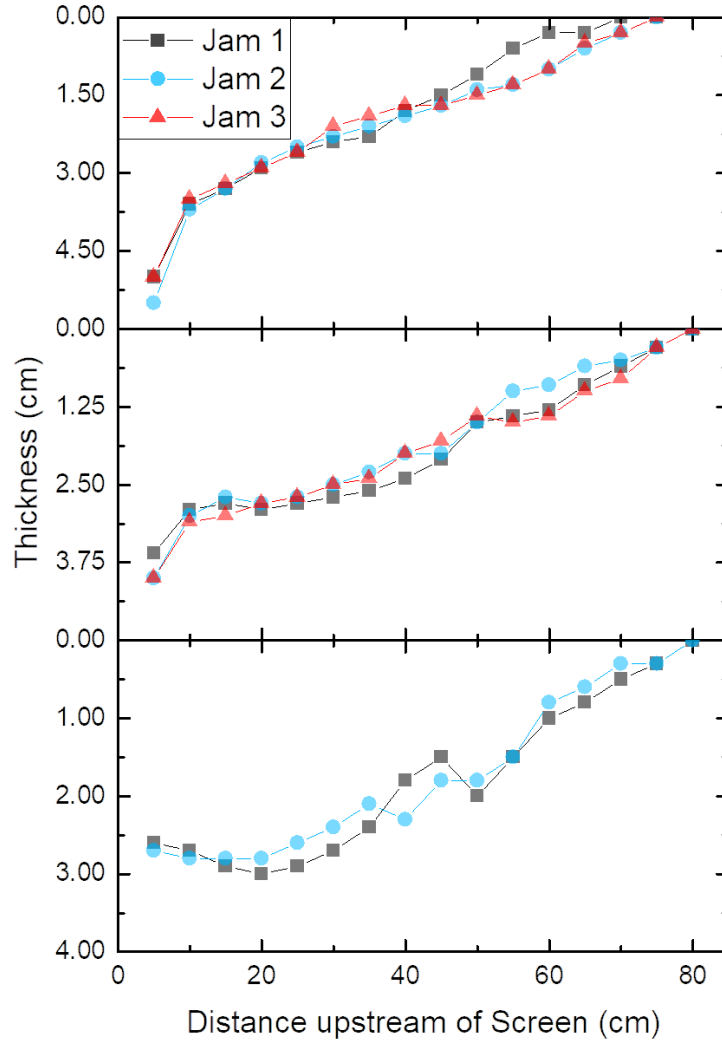


Figure 12 – Ruler-measured jam thickness for Case 15 (top), 10 (middle), and 5 (bottom).

The above process amounted to 18 planes of centerline velocity measurements. Four additional off-centre planes at the location of Plane 1 (1017 mm from the inlet) were captured during ice jam conditions to provide some insight into the characteristics of the secondary flow and its significance. The planes were taken at 20 and 54 mm offsets from the centreline of the channel for both the 15 and 5 cm test cases to examine the secondary flow at the lowest and highest aspect ratios, respectively. Important to note is that capturing each of the offset planes required

moving the camera, and therefore recalibrating the PIV scale factor. This meant the offset planes could not be taken in the exact same flow conditions as the centerline plane as calibration required removal of the jam, and with the camera being moved there was no way of quantifying any potential changes outside confirming the similarity of jam thicknesses. The jams were reformed as closely as possible after the new scale factor was found, the same way as was done during the primary tests. The summary of all test conditions and planes are shown in Table 1.

3.2.3 Test Conditions

For the primary analysis three test conditions were used, with varied flow depth being the primary variable considered. The tests were aimed to be at approximately 5, 10, and 15 cm of upstream water depth. Thickness profiles of the ice jam were attempted to be kept consistent between the three test cases, however the flow conditions at lower depths made it impossible to get the same levels of thickness as at the higher depth due to pellets being more prone to scouring from the underside of the jam. The differences in jam shape do not prevent this work from accomplishing its objectives, however, as the research aimed to relate seepage values to thickness, rather than to the distance along the ice jam.

The test cases were chosen to change the water level as the primary variable, rather than velocity or jam thickness. This was done to attempt to simulate the behavior of an ice jam approaching, but not reaching grounding. Additionally, the goal of relating seepage to relative thickness ($\frac{\text{jam thickness}}{\text{water depth}}$) means that a larger range of relative thickness values can be tested with the same size jam just by lowering water depth.

While upstream water depths were aimed to be 50, 100, and 150 mm, the actual steady state water levels after the jam finished increasing them did not end up at exactly these values. The

water depths, maximum jam thickness, and relative thicknesses tested are summarized in Table 2. The expected range of relative jam thicknesses was therefore from 0 (at the leading edge of all the jams) to 0.67 at the toe of the 5 cm test case, however more exact thickness values would be calculated after testing based on image processing algorithms as ruler measurements through the flume wall are not accurate enough for the analysis in this experiment. Open water Froude numbers were intended to be kept constant throughout all tests, at a value of 0.08. The velocities required to achieve this are shown in Table 2, however the flume was not equipped with any type of discharge measurement outside completing the actual PIV analysis, therefore the actual velocities achieved varied slightly from the desired velocities.

Table 2 - Summary of design test conditions.

Test Case	Measured Water Depth (mm)	Maximum Measured Ice Thickness (mm)	Maximum Relative Jam Thickness	Desired Froude # (U/\sqrt{gh})	Desired Velocity (m/s)
5	55	30	0.67	0.08	0.060
10	101	40	0.44	0.08	0.080
15	145	50	0.34	0.08	0.095

3.3 Data Processing

3.3.1 Adaptive Correlation

A spatial resolution test was performed for one plane testing a range of interrogation area sizes. The results showed that an interrogation area of 64 x 32 provided reliable results and could be used for the remaining analysis. While smaller dimensions would have provided more data points, they were found to have less reliability over the very long test duration while the data quality seemed to maintain for longer using the larger area. Increasing the x dimension to 64

rather than a square area of 32 pixels allows the process to find particles within the zone more reliably even with a degree of settling. Since the primary concern in this analysis is velocity profiles, it is more imperative to have detailed resolution in the vertical direction rather than the horizontal because velocity changes between vectors in the vertical direction more drastically than vectors in the streamwise direction. The 64-width interrogation area simply reduces the number of profiles that are available to analyze. The maximum field of view therefore resulted in a vector field of 63 x 127 vectors, each representing a physical area of 2.52 x 1.26 mm, however in the lower depth cases a significant portion of the image was either above the water surface or below the bed and was therefore excluded from the correlation to improve processing time and reduce storage requirements.

3.3.2 Post-processing code

To translate the velocity fields generated by the adaptive correlation to a more useful format, the results were exported from DynamicStudio into a series of MATLAB data files. A set of MATLAB scripts developed in-house was used for post-processing velocity data, extracting mean velocities and turbulence statistics for all planes. This code created a data file to import these statistics to the Tecplot 360 software used for flow visualization, and also created a set of Excel files containing profiles of each of these statistics.

3.3.3 Thickness Measurement

While the thickness profile of every ice jam was measured using a ruler against the flume, this method would not be sufficient for any calculations involving ice thickness, as with the “hills” that form the underside of the ice jam there is no guarantee that the thickness at the wall – where

the ruler can measure – is the same as the thickness at the centerline. As all velocity data and calculations are taken at the centerline, a new method for thickness measurement was needed.

Since the result of PIV work is a set of images of the jam, where a scale factor relates the pixels in an image to real-world coordinates, these images could be used for finding the jam thickness based on pixel measurements. When the light passes through the acrylic floor of the channel, a small bright line is visible where the laser sheet enters the water, as it illuminates whatever small particles are stuck to the bed. Similarly, when the laser sheet exits the water at the open water surface, another brighter line is visible in the image. Both lines can be used to visually find the water surface and channel bed from an image. Lastly, when under the ice jam, the laser sheet illuminates a line at the center of the jam. This is visible as large bright areas in the PIV images, and the center of this bright curve represents the bottom of the ice jam surface at the centerline. These bright areas can all be used to visually locate the water boundaries from the PIV images. Doing so manually would be time intensive and subjective, so an image processing script was created in MATLAB to analyze the images captured by the PIV camera to determine the locations of the channel bed and of the underside of the ice jam.

A single grayscale frame of each of the 6 planes of a test case was loaded and stitched together to form a single ice jam profile image. Vertical slices with width equal to the interrogation area width were analyzed in sequence to find the brightest spot on the top and bottom halves of the slice. In order to have the entire flow depth under the ice jam visible to the camera, it must be the case that the bed is in the lower half of the image, and the underside of the ice jam must be in the top half.

The image processing algorithm first applied a Gaussian filter to the image. As the illuminated particles in the flow are also very bright due to the nature of PIV, they could potentially be detected as the brightest part of the image. However, since the particles are very small relative to the bright areas at the bed and the jam, a blur applied to the entire image removes the particles and ensures a bright particle is not mistaken for the bed or jam location. Next, for each of the top and bottom halves of slices, a threshold filter is applied to create a binary image, with values of 1 for any pixel above the threshold value. This value is then slowly increased until only the one brightest spot in the slice remains, at which point the center of this bright spot is recorded as the point of interest. A check is then performed on the new data point for whether it is too far away from the neighboring data points, then corrects any elevations which are unreasonable so that the ice jam thickness changes smoothly throughout the profile. In a select few cases, which can be seen in Figure 13 in Case 10 particularly, the estimated top elevation was clearly incorrect and was fixed manually afterward, however in most locations the algorithm placed the elevations accurate enough compared to where one would expect them to be by visual inspection.

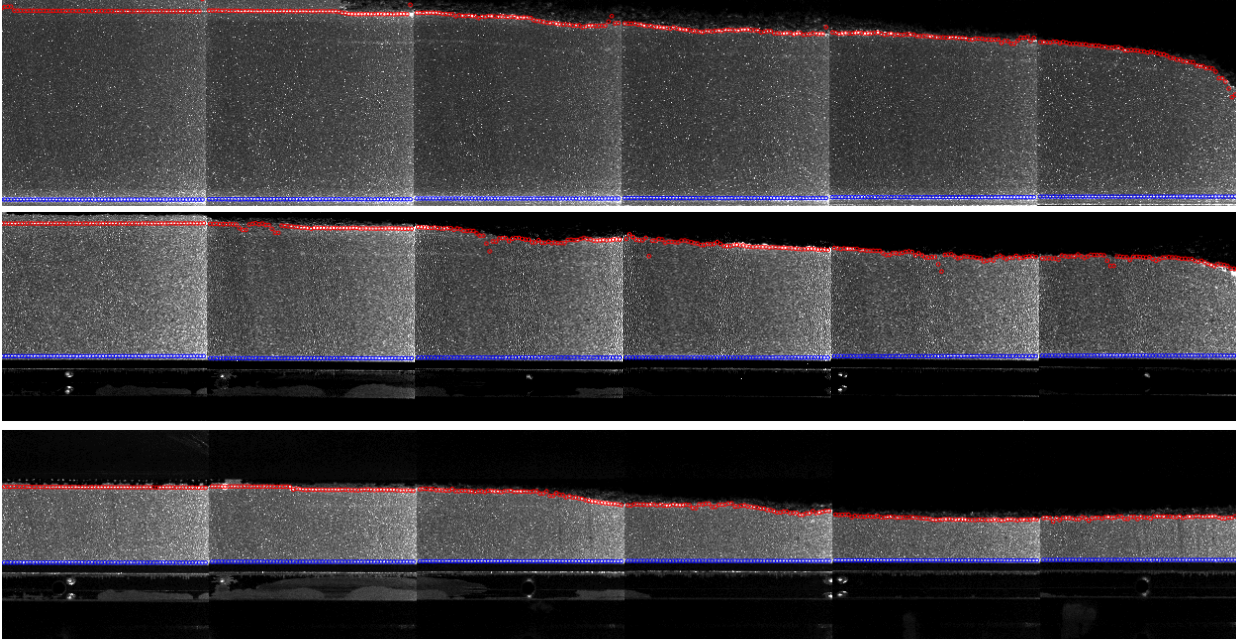


Figure 13 – Top (red) and bottom (blue) elevations from image processing for Case 15 (top), 10 (middle) and 5 (bottom).

After calculating all these points (shown in Figure 13) open water depth is calculated by averaging the differences in all the slices in the open water plane. Ice thickness is then calculated at all points where the water depth is less than the open water calculation by equation 20, where t_i is the calculated ice thickness at any streamwise location n , s_i is the specific gravity of the model ice, and h_{open} and h_{under} are the open water and under-ice depths respectively.

$$t_{i,n} = \frac{h_{open} - h_{under,n}}{s_i} \quad 20$$

The results of this process are represented in Figure 14.

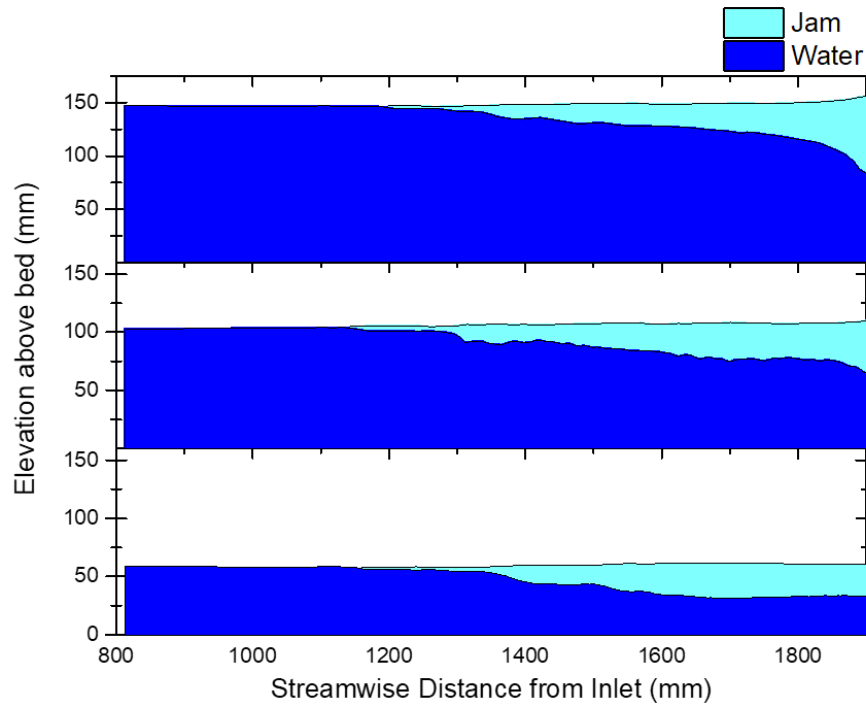


Figure 14 – Calculated ice jam thickness profiles from image processing for Case 15 (top), 10 (middle), and 5 (bottom).

To evaluate the accuracy of this method, the calculated open water depths and ruler-measured depths are compared in Table 3. There is no way of quantitatively comparing the accuracy in ice thickness measurements as ruler measurements could not be taken at the centerline, however in the open water the results were very close, with only between 2 and 4 mm difference between the measured and calculated values.

Table 3 - Comparison of measured and calculated water depth.

Test Case	Open Water Depth (mm)		Error	
	Ruler Measured	Calculated from Image Processing	Absolute Difference (mm)	Percent Difference
5	55	58.5	4	6
10	101	103.0	2	2
15	145	146.9	2	1

4 Results and Analysis

4.1 Flow Conditions

4.1.1 Overview

The test condition summary in Table 2 shows the intended flow conditions, and best efforts were made to conform to these. However, since the flow conditions could only be precisely known after the data processing was complete, it was expected that the actual values would not match with the experimental design.

Table 4 shows the actual recorded flow conditions for the upstream plane of each test case. Open water depth was measured from image processing (as in Table 3) and streamwise velocities (U) were averaged over the entire flow depth. Froude numbers were calculated to be slightly lower than the design value of 0.08, likely due to the “quick test” velocity checks used to set up the experiment being based off the faster free stream velocities rather than an average velocity that includes the slower bed region. However, the three tests are still comparable as the Froude values were still very close in each case.

Table 4 – Summary of recorded flow conditions.

Test Case	Ice Volume (L)	Average Velocity (m/s)	Open Water Depth (mm)	Froude Number (U/\sqrt{gh})	Reynolds Number ($\rho UR/\mu$)
5	2.50	.056	58.5	0.075	2083
10	3.00	.074	103.0	0.074	3768
15	3.25	.090	146.9	0.075	5318

4.1.2 Average Velocities

The following section features several contour plots representing the different flow statistics calculated by the postprocessing code described in section 3.3.2. All contour plots are shown in the same format, with all three test cases (15 cm, 10 cm, and 5 cm depth) displayed from top to bottom and all 6 planes of each case shown left to right. These plots are intended to display the ice jam as it was visible to the camera, with all scaling kept consistent in the X and Y directions. Normalized data is then shown in the following profile plots. A gap exists after plane 1 as this plane was located further upstream from the jam rather than being directly adjacent to plane 2. The same coordinate system applies to all contours as well, with the x axis representing the streamwise distance from the channel inlet in and the y axis representing the height within the camera's field of view, both in mm. The results shown have also been trimmed based on the calculated top and bottom elevations determined through image processing. As the captured images contained no seeding particles outside the water depth or within the jam, the velocity data in this region contained random vectors, and these needed to be set to zero and trimmed from the dataset to not affect seepage calculations later.

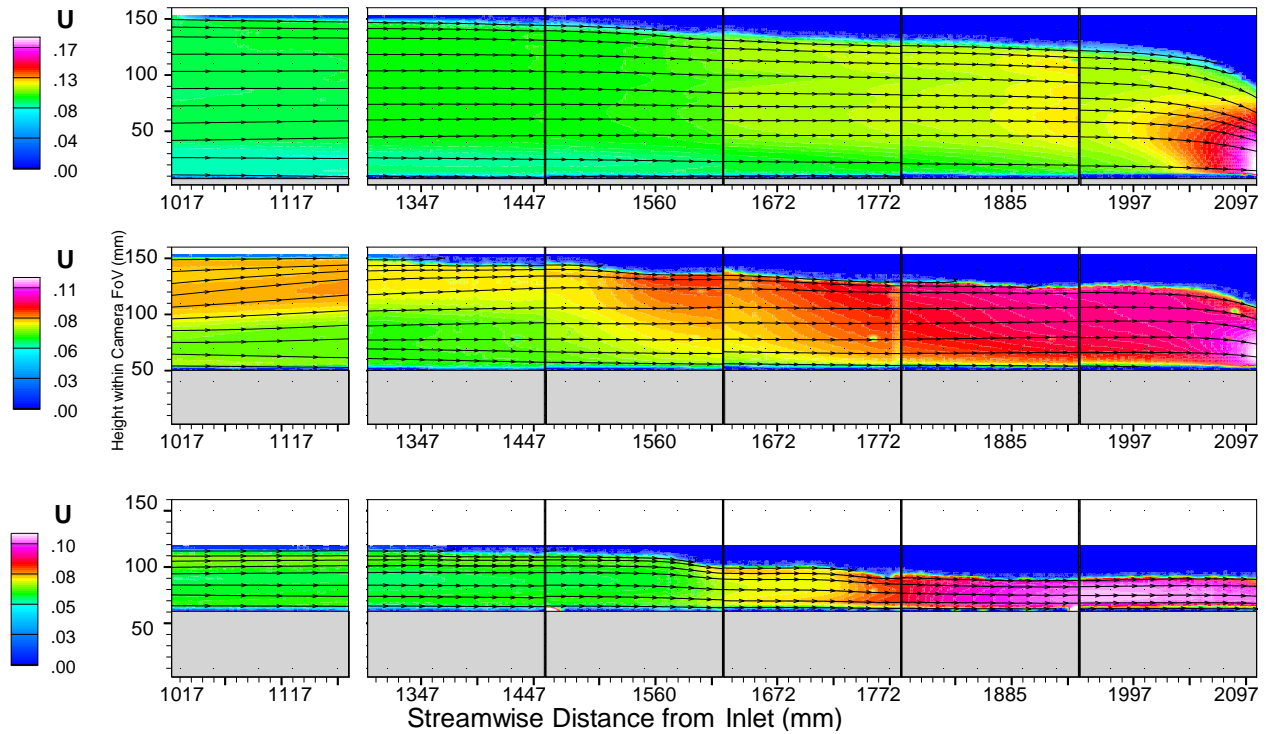


Figure 15 - Average streamwise velocity (U , m/s) contours with streamlines for Case 15 (top), 10 (middle), and 5 (bottom).

Figure 15 shows the streamwise velocity contours of the three test cases. In all cases the regions with the highest velocities were at the thickest areas of the jam near the toe, as could be expected based on past research (Pahlavan, 2016; Nyantekyi-Kwakye, et al., 2018). In the 5 cm test case the maximum velocity was not at the most downstream location as the jam reached its maximum thickness before that point and maintained a fairly constant thickness until the end of the profile, as scour prevented the jam from thickening further. It is particularly useful to see the streamtraces shown nearest to the ice jam. In each of the test cases, some streamtraces could be seen to redirect upward into the ice jam at a few locations. The portion of flow in voids must approach 100% as the jam approaches grounding, so this is a simple check to see that some of the under-ice flow was in fact becoming seepage flow as the jam becomes thicker.

Of note are the small discontinuities visible from planes 3 to 4 and 5 to 6, primarily visible in the 15 cm test case. As there was a short time available before particle settling impacted data, only two planes were captured before cleaning the channel and remaking the jam, and the discontinuity occurs at the interface of planes where the jam was reconstructed between captures. While the approximate velocities were checked before accepting the new jam, it was never expected that precisely the same conditions would occur twice. Regardless, the actual differences in value at these interfaces is small – around 3% in most cases and 8% in the worst case – and exaggerated by the wide spectrum colour scale.

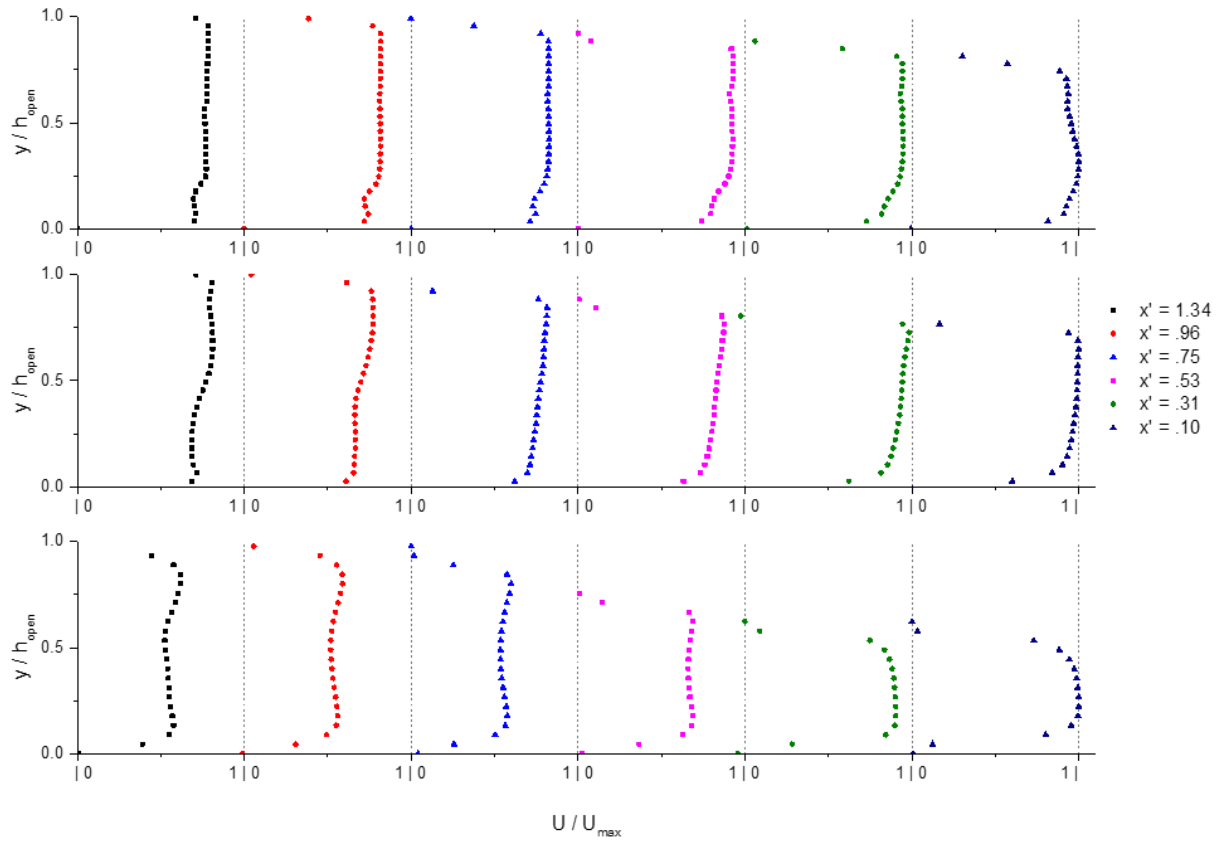


Figure 16 – Normalized streamwise velocities for Case 15 (top), 10 (middle), and 5 (bottom).

Figure 16 shows the streamwise velocity profiles at selected locations along the channel, normalized by the maximum velocity from all planes (U_{max}) and each scaled from 0 to 1. One profile was taken from near the center of each plane. The location of the profiles (x') are represented as the distance upstream of the screen normalized by total jam length, where $x' = 0$ represents the screen and $x' = 1$ is the leading edge of the jam. Vertical axes for each plot show height above the bed (y) normalized by the open water depth of that test (h_{open}). The same y-axis and profile locations will be used for every similar plot in this section.

It can be seen in Figure 16 that flow in the channel was never fully developed, as all profiles often featured a single similar value over a range of depths with the maximum velocity occurring over this flat region of the profile. In contrast, if the flow were to follow power or log laws (Equations 8 and 9) a single maximum velocity at the peak of a curve would be expected. Running the flume with no jam did show fully developed flow at that location as was expected. The lack of fully developed flow in the ice jam tests will be discussed in later sections but could not be avoided with this setup, despite the efforts put into facilitating boundary layer development and fully developed flow being seen when the ice jam is not present, and also seen in previous constructed ice jam work in the same flume (Nyantekyi-Kwakye, et al., 2018). Some expected trends in the velocity profiles are apparent, with velocities increasing as the jam thickens and the maximum velocities occurring in the last plane – the jam toe – in each of the test cases. The location of the maximum velocity would also be expected to move downward, especially in the case of a rough ice jam and smooth bed. This is visible to a degree, especially in Case 5, but the lack of fully developed flow prior to the jam masks this behaviour somewhat as there is no obvious location of maximum velocity upstream to compare to the downstream profiles.

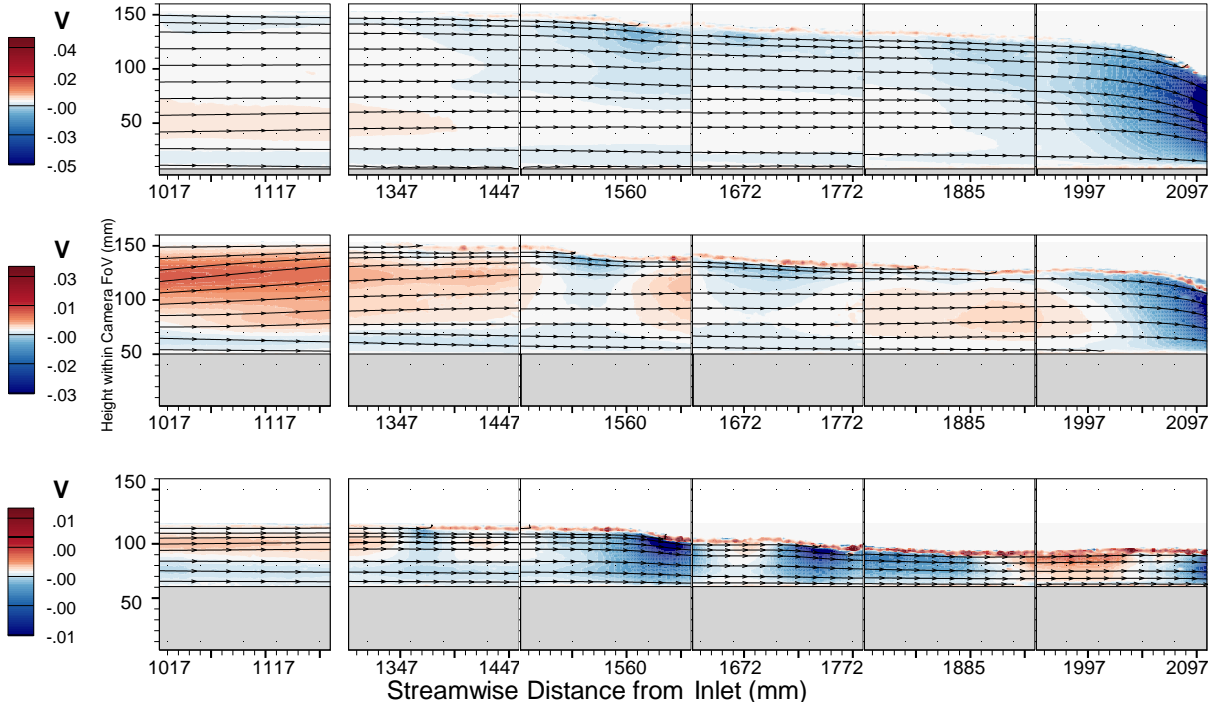


Figure 17 - Average vertical velocity (V , m/s) contours of Case 15 (top), 10 (middle), and 5 (bottom).

Figure 17 shows the distribution of mean vertical velocities along the jam profiles. The colour scale shows upward velocities as red and downward velocities as blue. It is first worth noting that the colour scale is meant to exaggerate these velocities, with any small deviation from 0 resulting in a shade of red or blue, to clearly highlight the areas where the flow direction changes. In general, the magnitude of all V velocities shown in Figure 17 and Figure 18 are extremely small relative to those seen for U in Figure 15, with maximum V on the order of .05 m/s compared to .17 m/s for U . In all three test cases, V remained relatively close to 0 throughout most of the profile, with relatively large downward velocities occurring at the toe in each case, as was to be expected by the sharper increases in thickness near the screen. However, upward velocities were present, most visibly in the 10 and 5 cm cases. These occur in any areas where

the jam's thickness profile was relatively flat and disappear in areas where the jam is thickening and forcing flow downward. Based on the very low aspect ratios ($\frac{width}{height}$) of the flow area – from 1.4 in the 15 cm case to 3.4 in the 5 cm case – some secondary flow was to be expected in the channel. The assumption of 2-dimensional flow is often made at very high aspect ratios (>10) and there was no practical way to achieve such a value in this experiment, so 3D flow was expected.

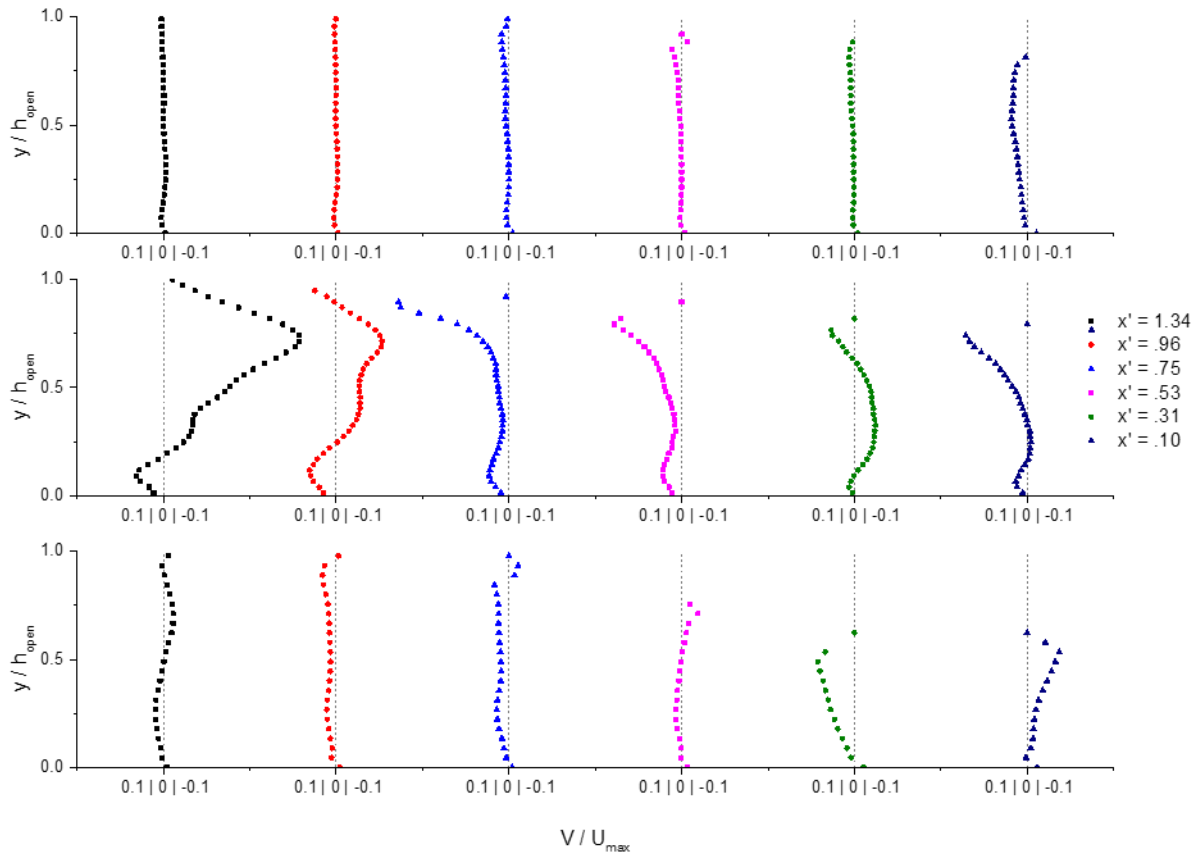


Figure 18 – Vertical velocity profiles normalized by U_{max} for Case 15 (top), 10 (middle), and 5 (bottom).

Figure 18 shows selected V velocity profiles, with each subplot centered on a value of 0 and scaled between -0.1 and 0.1 times U_{max} . In each test case the values are often negligible compared to the streamwise component. The 15 and 5 cm cases show values are generally near zero with some negative values where the water is moving downward as the jam thickens. In the 5 cm case there are some regions of positive (upward) motion in the flatter sections corresponding to the red secondary flow cells in the contour diagram. The largest values are in the 10 cm case which appear to have the strongest secondary circulation upstream with V values on the order of 5% of U_{max} . It also has the strongest downward velocities near the bed, although it remains a very small value. The secondary flow cells in this case likely have the same shape and direction as those in the 5 cm case, however due to the much higher flow depth in the channel the positive top region is larger.

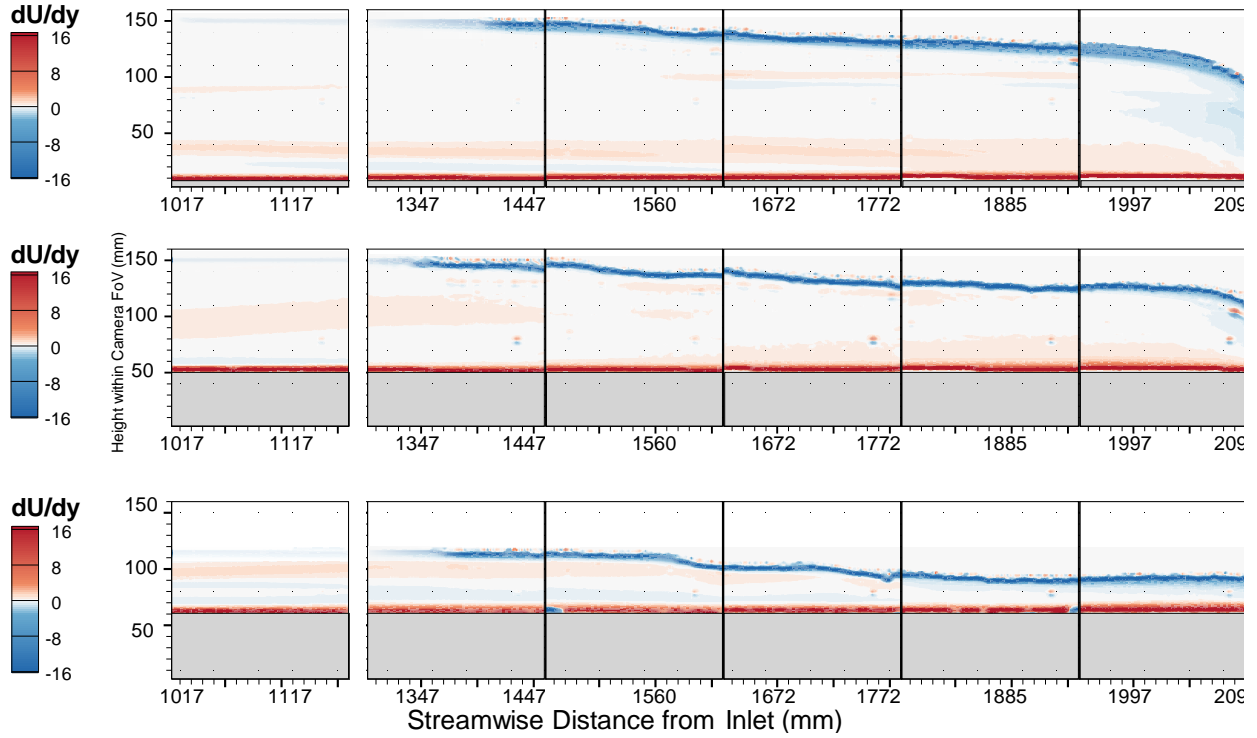


Figure 19 – Mean shear contours (dU/dy , s^{-1}) of Case 15 (top), 10 (middle), and 5 (bottom).

Figure 19 shows the change in streamwise mean velocity over height (dU/dy), which is directly related to the average shear stress according to equation 6. The values near the bed and ice jam are expected to be much higher than further in the flow area. Of greater interest is the small values outside of the boundary layers which, with fully developed flow, would be expected to be positive near the bed until the location of maximum velocity, and negative in all areas above the maximum velocity. Instead what we see in Figure 19 (most visibly in the 5 cm test case) is a thin section of negative (blue) values just above the bed that persists until partway down the jam. This corresponds to the small bump in U velocities that can be seen near the bottom of the channel in the upstream profiles of Figure 16, with small secondary peaks in velocity. A potential cause of this behaviour is the fast moving free-stream region remaining distinct from

the developing boundary layer, with the increasing ice jam depth forcing the free-stream region downward and impeding the development of the boundary layer.

Figure 19 is also useful for diagnosing areas of erroneous data such as those caused by reflections or overexposure, as these may appear as insignificant changes to the mean velocity contours but form visible “bubbles” of adjacent positive and negative values for dU/dy . The most significant of these is the small spots of reduced velocity that can be seen in the centre-right of each plane. Each of the PIV images had a small dark dot in this region which caused particles to be less visible for cross-correlation. Other anomalies visible in this figure are areas where data was affected by reflections of the laser off the far wall of the flume. These appear as small traces of red and blue following just underneath the outline of the jam, most notably visible in plane 2 of the 10 cm test case.

4.1.3 Turbulence

The Reynolds numbers (Re) recorded in the experiment were 2083, 3768, and 5318 for test cases 5, 10, and 15 respectively. Based on a critical Reynolds number for open channel flow, where flow is laminar at $Re < 500$ and turbulent when $Re > 1000$, (Lowe, 2003) all test conditions remain in the turbulent regime. This is noticeably lower than flows in past PIV-based ice jam work, (Nyantekyi-Kwakye, et al., 2018) however is unavoidable as in this experimental setup the velocities and jam formation are interdependent, rather than velocity being a defined value forced under a specific jam geometry.

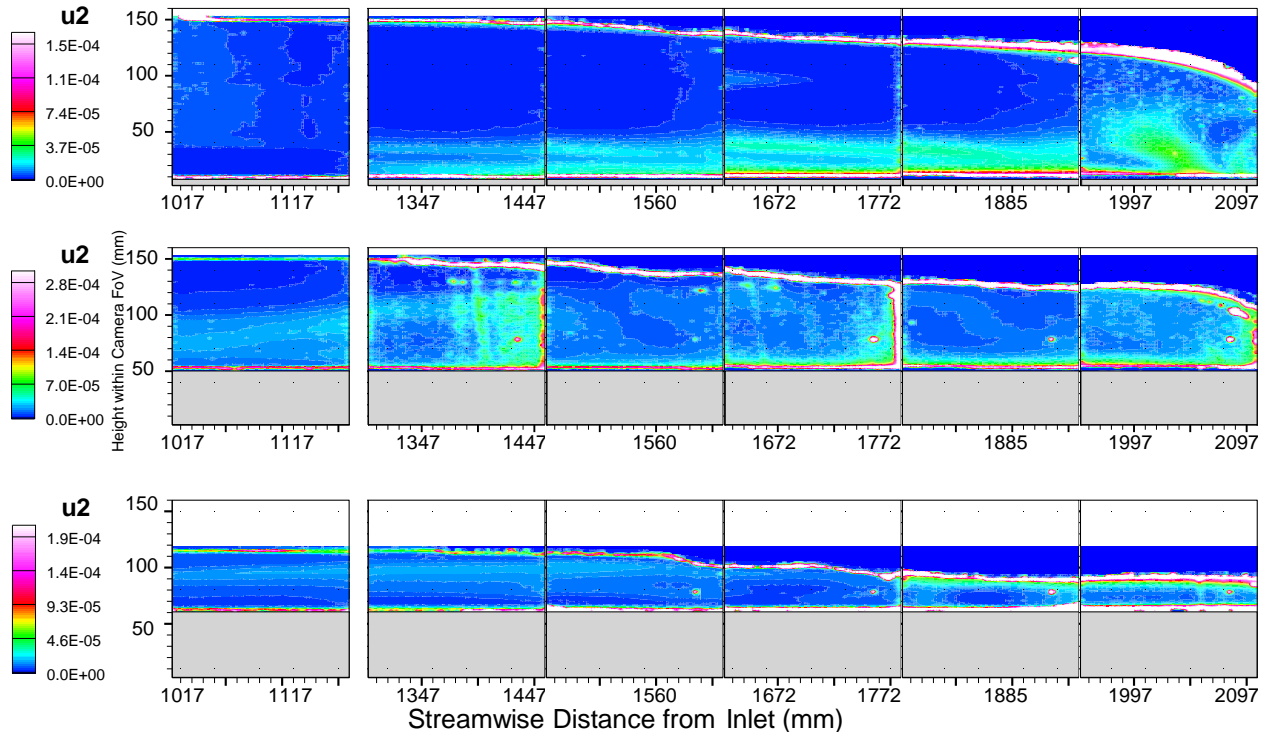


Figure 20 – Streamwise Reynolds stress ($u^2, m^2/s^2$) of Case 15 (top), 10 (middle), and 5 (bottom).

Figure 20 shows contours of the computed streamwise Reynolds stress, $\overline{u^2}$. The most obvious characteristic of these plots are the streaks and scattered dots visible in some of the planes. These are most noticeable in the 10 cm test case, where alternating planes showed very poor data quality – a condition seen in previous work when the recording time was long enough for particle settling to noticeably reduce seeding density. Plane 6 of Case 15 also shows erroneous data, however the other planes, as well as Case 5, seem to show consistent results. However, as expected by the relatively low Reynolds numbers used in this experiment, most of the flow area has either very small or near-zero values for $\overline{u^2}$, with maximum values on the order of 5.0×10^{-5}

m^2/s^2 within the primary flow area, however little prior research had been published to which these Reynolds shear stress values could be compared.

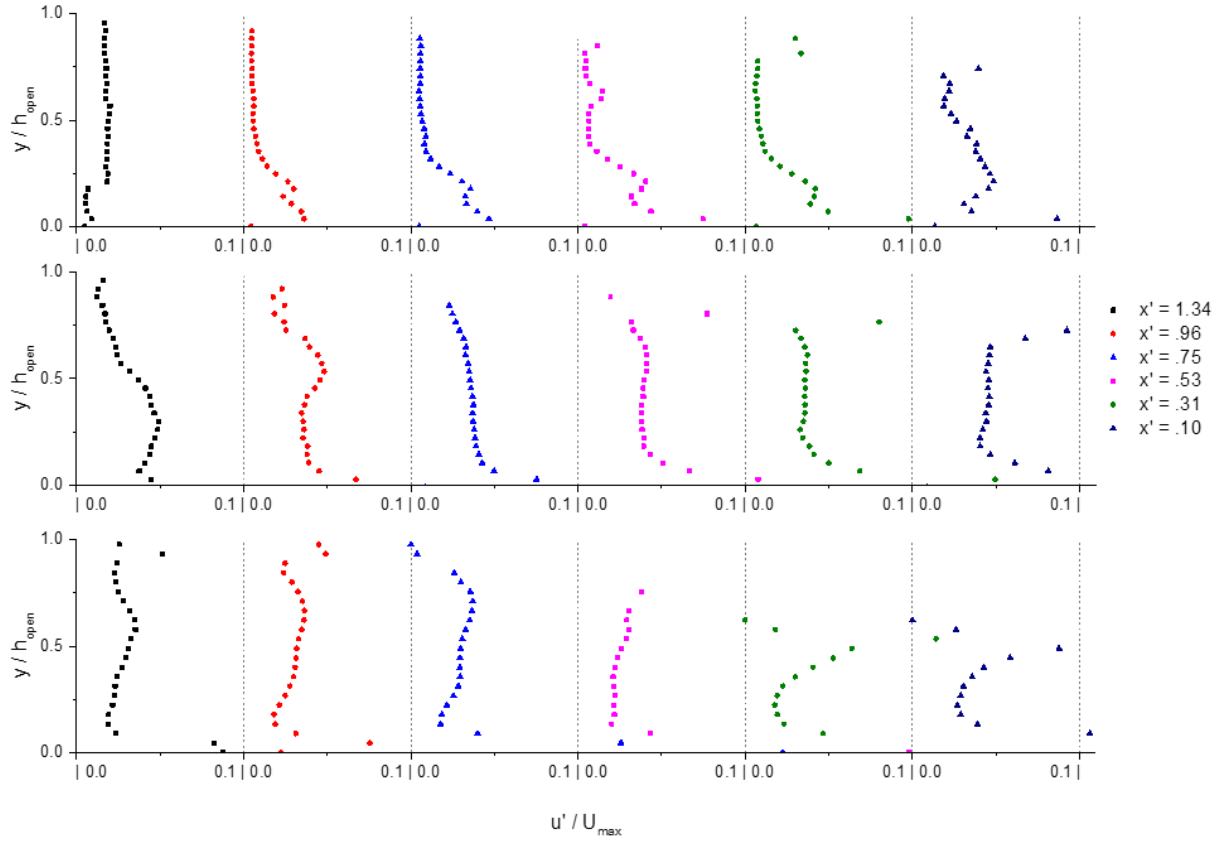


Figure 21 – Streamwise turbulence intensity normalized by U_{max} for Cases 15 (top), 10 (middle), and 5 (bottom).

Figure 21 shows the streamwise turbulence intensity profiles normalized by U_{max} , with one profile from each plane as with the previous profile plots. The turbulence intensity values are scaled from 0 to 10% of U_{max} in each series, with most of the points remaining at the lower end of that range, around 3-5% of U_{max} . A thin peak in u' can be seen near the bed in all cases, as

would be expected with a smooth bed based on past research (Nyantekyi-Kwakye, et al., 2018). Another less pronounced peak is visible directly under the jam in profile which is also expected based on the same research. For the open water plane, we would expect the u' profile to feature a large bump near the bed which decreases toward the surface (Nezu & Nakagawa, 1993) which somewhat appears in the 10 and 5 cm case, however is not well aligned with what would result from equation 9.

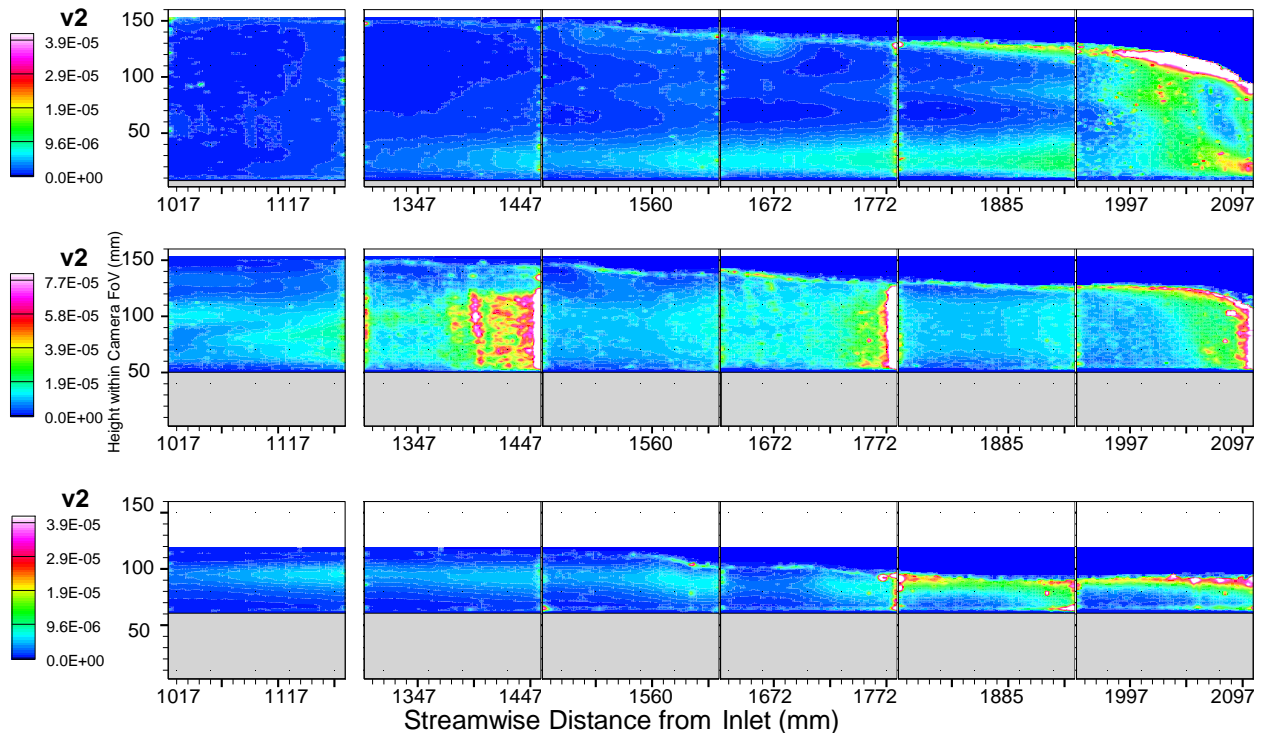


Figure 22 – Wall-normal Reynolds stress (v^2 , m^2/s^2) of Case 15 (top), 10 (middle), and 5 (bottom).

The vertical component of Reynolds stress is shown in Figure 22. The same areas of erroneous data as in Figure 20 are apparent. As with the streamwise components, at most locations the values for $\overline{v^2}$ are very small, being mostly in the blue ‘near-zero’ range except under the thickest

parts of the jam in Cases 15 and 5. The colour scale of this graph is also lowered to accentuate the small regions where $\overline{v^2}$ does increase, such as near underside of the Case 5 jam.

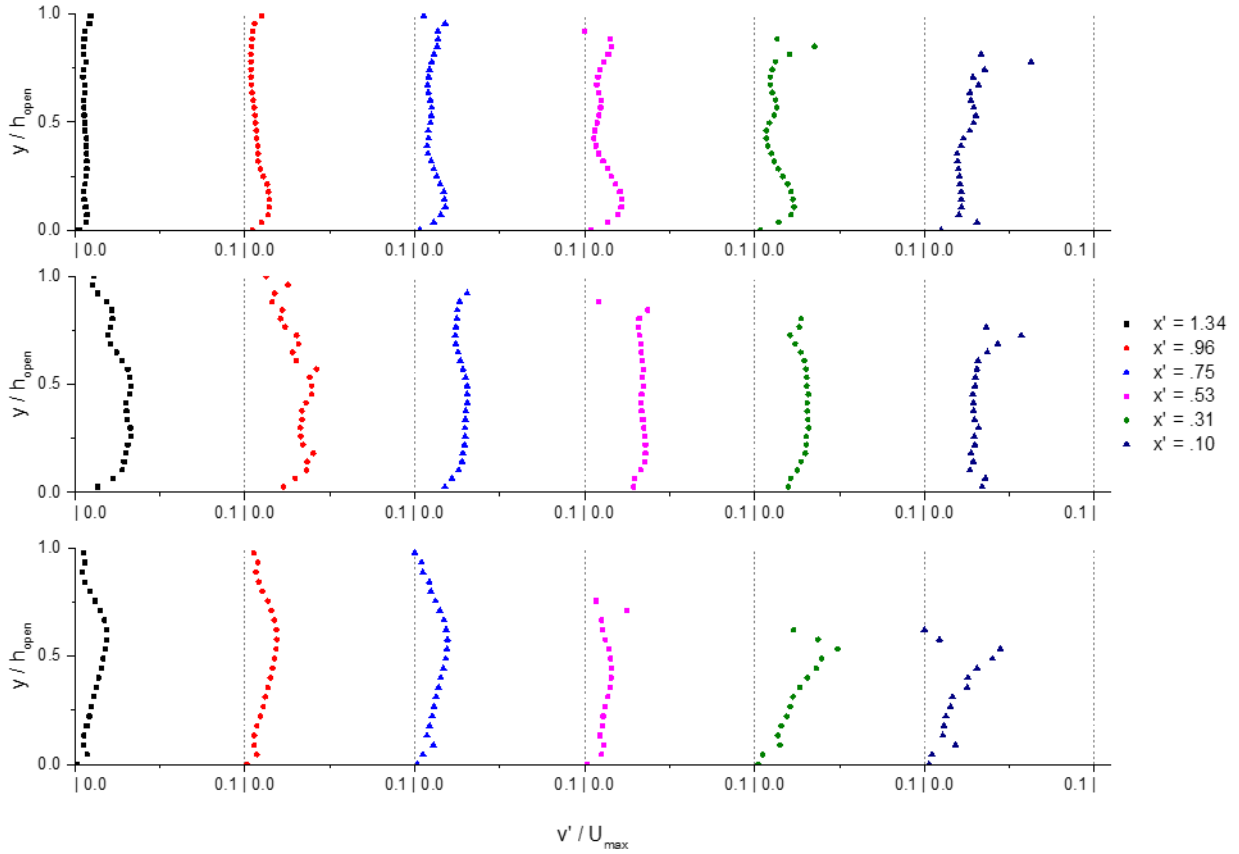


Figure 23 – Normalized vertical turbulence intensity for Cases 15 (top), 10 (middle), and 5 (bottom).

Profiles for the vertical turbulence intensity, again normalized by U_{max} , are shown in Figure 23. These remain at very low values throughout, generally around 2% of U_{max} and never exceeding 10%. The most significant trends are the spike in intensity that occurs directly underneath of the jam in each case due to the roughness of the jam, the magnitude of which seems to increase as it

progresses downstream likely due to the jam thickening and involving higher mean velocities at the location of profile. Excluding some profiles in Case 10 (which were in the erroneous data regions) every profile approaches zero at the bed, as would be expected by the impermeable boundary. It does not approach zero at the jam underside, and while vertical velocities can exist here due to flow exchange into the jam voids, they are still very small. The lack of a ‘zero’ value at the jam is more likely attributed to the inability of recording accurate vectors very close to the interface, as this is where the laser collides with the ice pellets and creates an overexposed line in the image pairs. The spikes in $\overline{v^2}$ seen just underneath of the jam, however, are outside of this bright area and are reasonable to expect as the flow would experience more variance in its vertical velocities as it flows over the rough jam underside.

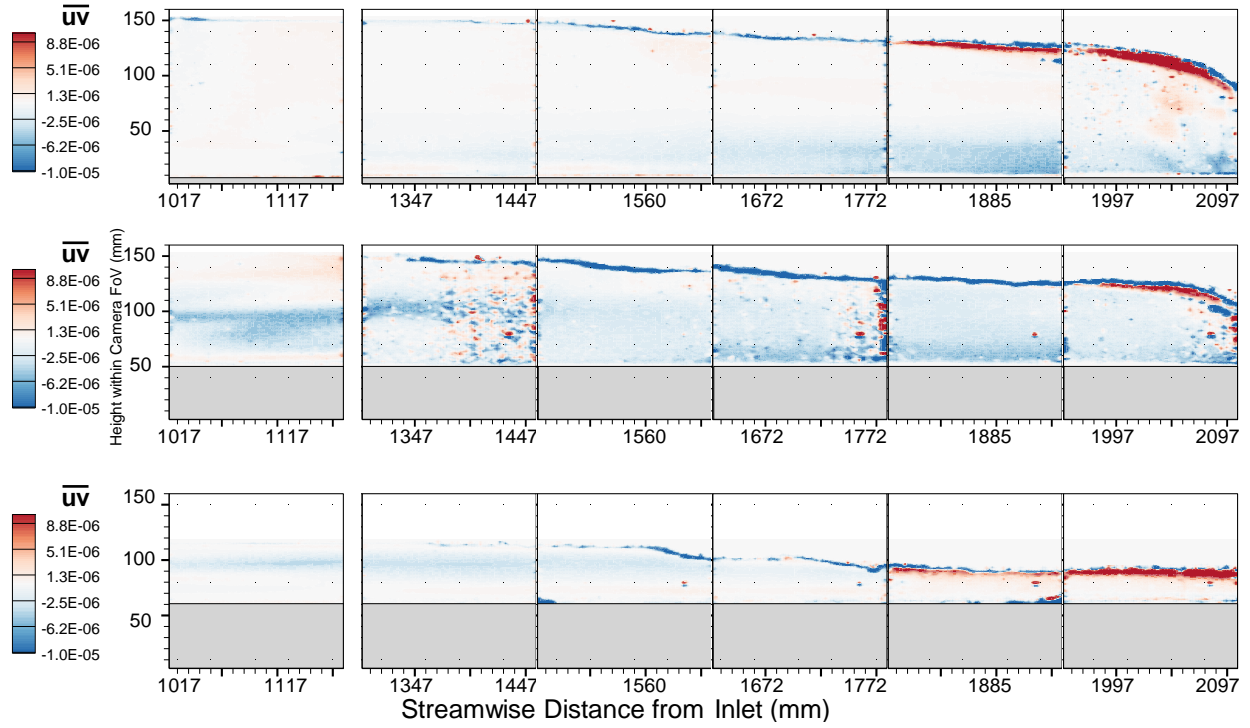


Figure 24 – Reynolds shear stress (\overline{uv} , m^2/s^2) contours of Case 15 (top), 10 (middle), and 5 (bottom).

The last turbulence statistic calculated was Reynolds shear stress, or \overline{uv} , with contours shown in Figure 24 and profiles shown in Figure 25. Within the contour plots, the colour scale again shows positive values in red and negative values in blue to accentuate these regions, however the values again are all very close to 0, as emphasized by the profile plots below. Exceptions to this exist only in a few small peaks nearest to the underside of the jam.

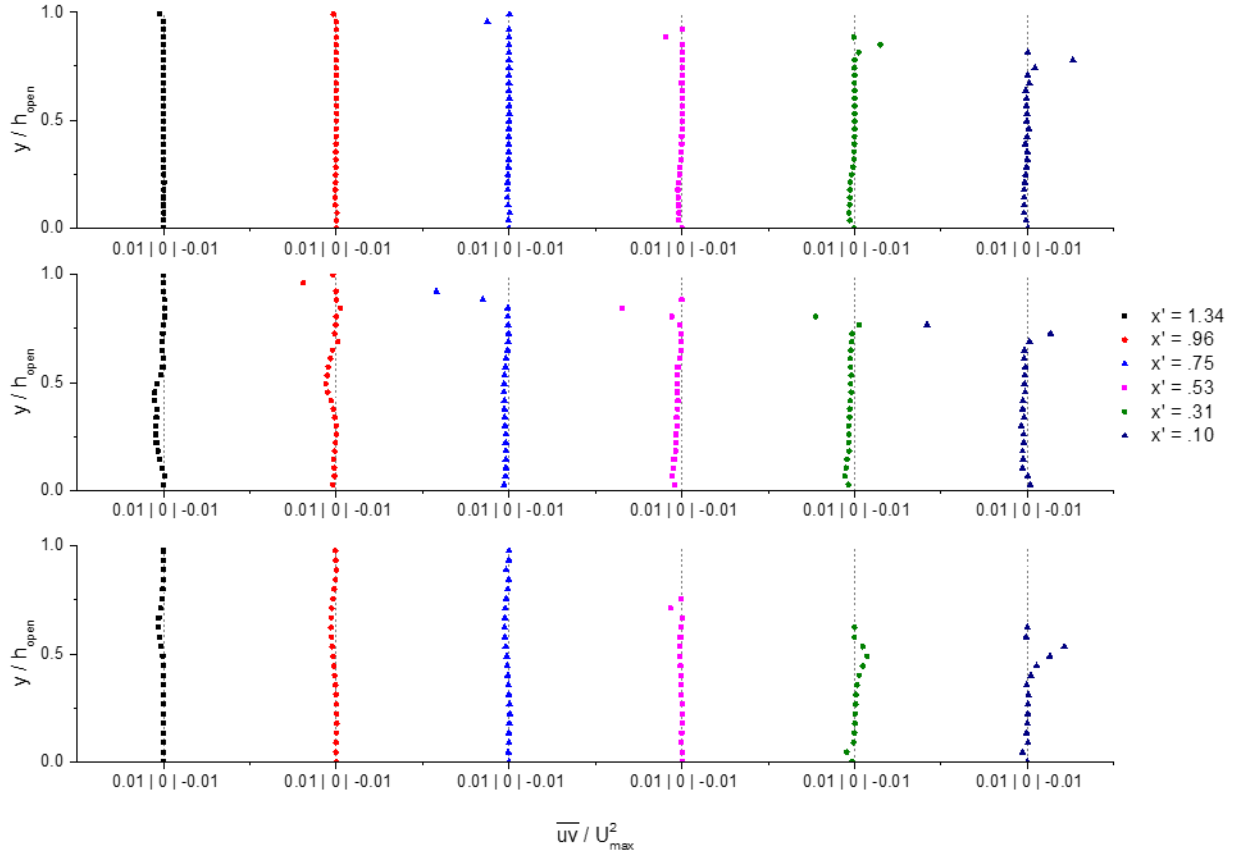


Figure 25 – Reynolds shear stress normalized by U_{max}^2 for Cases 15 (top), 10 (middle), and 5 (bottom).

4.2 Void Seepage

Equation 21 can be used to find the flow at any given profile along the PIV capture plane, where q is specific discharge in m^2/s , U is the streamwise average velocity in m/s , and y is the flow depth in m . This equation is valid when assuming 2-dimensional flow, however the validity of this assumption will be analyzed and discussed later. Equation 22 represents this same concept, only discretized and summed over a column of streamwise mean velocity vectors with height m ,

solved at any streamwise location n . In this equation, Δy is the vertical spacing of vectors, being 1.268 mm for the centerline planes in this experiment. This equation was scripted in MATLAB to calculate q_n at every streamwise location in the PIV dataset.

$$q = \int U dy \quad 21$$

$$q_n = \sum_{i=1}^m U_{n,i} \Delta y_i \quad 22$$

The raw results from this process, shown in Figure 26, provided a large number of data points, but they were fairly scattered, as the discharge calculations at many locations were affected by reflections or proximity to plane edges. The data required some filtering before any useful trends could be seen. The following steps were performed to correct the dataset:

1. Trim plane edges
2. Correct data anomalies
3. Correct velocities for continuity
4. Apply smoothing filter

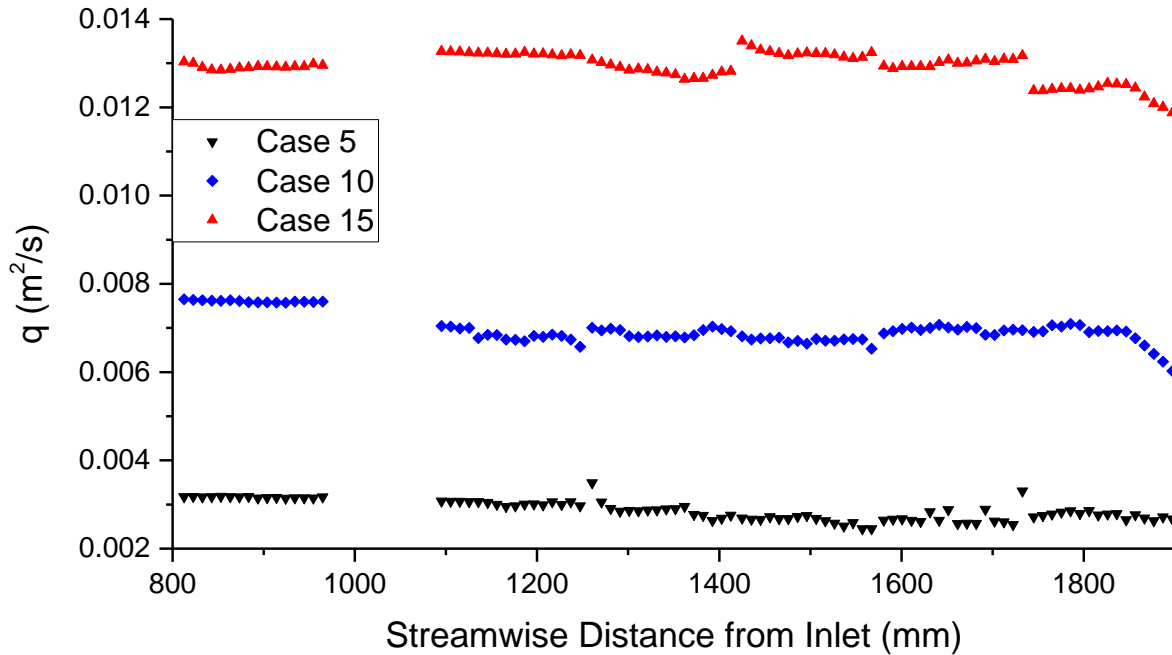


Figure 26 - Calculated specific discharge values along channel using equation 22.

As could be seen in the contour plots – such as in Figure 22 – the left and right edges of each plane all had a small width of poor-quality data. Typical PIV analysis would avoid using the extremes of the camera field of view in analysis for this reason. These areas showed spikes in discharge data, as seen in Figure 26, and were removed from each side of each plane. Next the continuity between planes was examined, as slight differences between each formation of the ice jam caused slightly different flume discharges. While the differences in peak velocities were very close in each jam reconstruction (generally within 3 to 5%), small discrepancies became more significant once the velocities were integrated over the entire depth, resulting in calculated discharges to have visible differences between planes in the same test. This can be seen in Figure 26 where the adjacent planes may have the same trend along the flume, however between planes where the jam was reconstructed the data appears to be simply moved up or down by a constant

amount. These were corrected by averaging the discharge points closest to the boundaries between planes, then factoring all velocities in the second plane until these average matched to maintain conservation of mass between the planes. The corrected specific discharge values are shown in Figure 27.

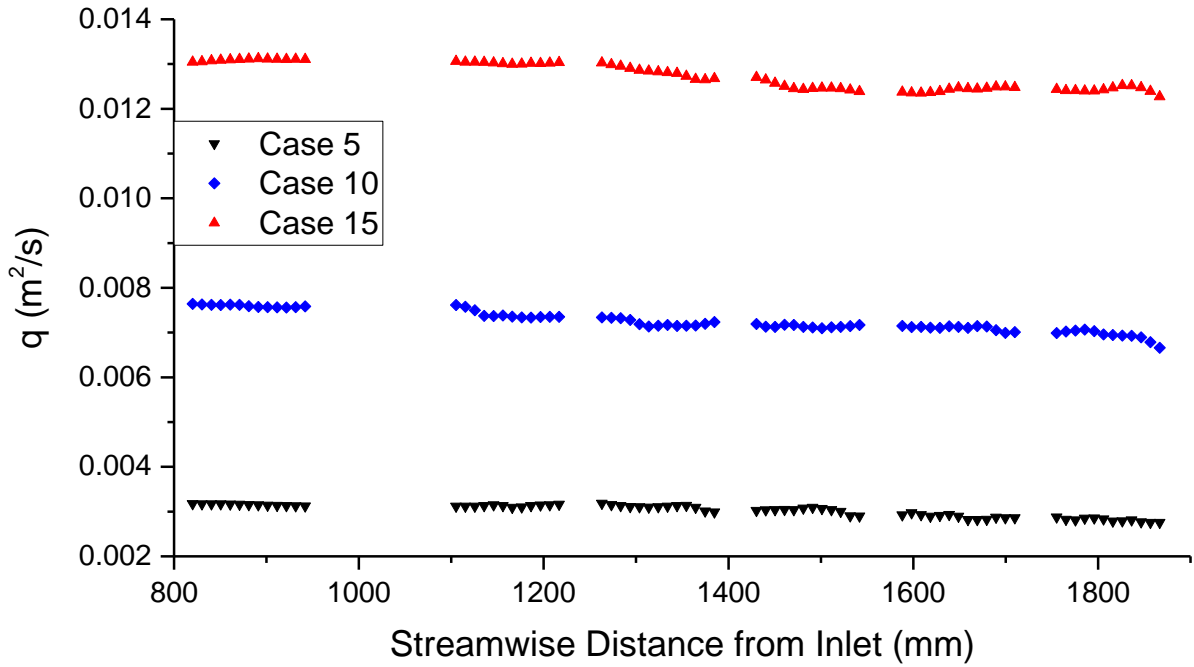


Figure 27 - Corrected specific discharge values along channel

The open water specific discharge – q_{open} – was calculated by taking the average of the integrated q values for all the profiles in the upstream-most plane. Then these values were compared to the calculated q values for every location in which the image processing script determined that ice thickness existed according to equation 20 to determine q_{voids} , the portion of the flow which is now flowing through the jam rather than under it.

$$q_{voids,n} = q_{open} - q_n \quad 23$$

Resulting from this series of MATLAB scripts is an array of q_{voids} values, in m^2/s , at all n locations in the streamwise direction. Nondimensional variants of these values can be created by comparing q_{voids} to the open water discharge in the test case, shown in Figure 28, and ice thickness to the open water depth according to the following equations:

$$Seepage\ Ratio_n = \frac{q_{voids,n}}{q_{open}} \quad 24$$

$$Thickness\ Ratio_n = \frac{t_{i,n}}{h_{open}} \quad 25$$

With these values calculated at every point, the percentage of flow moving through the jam can be compared to the percentage of flow area being occupied by the ice jam.

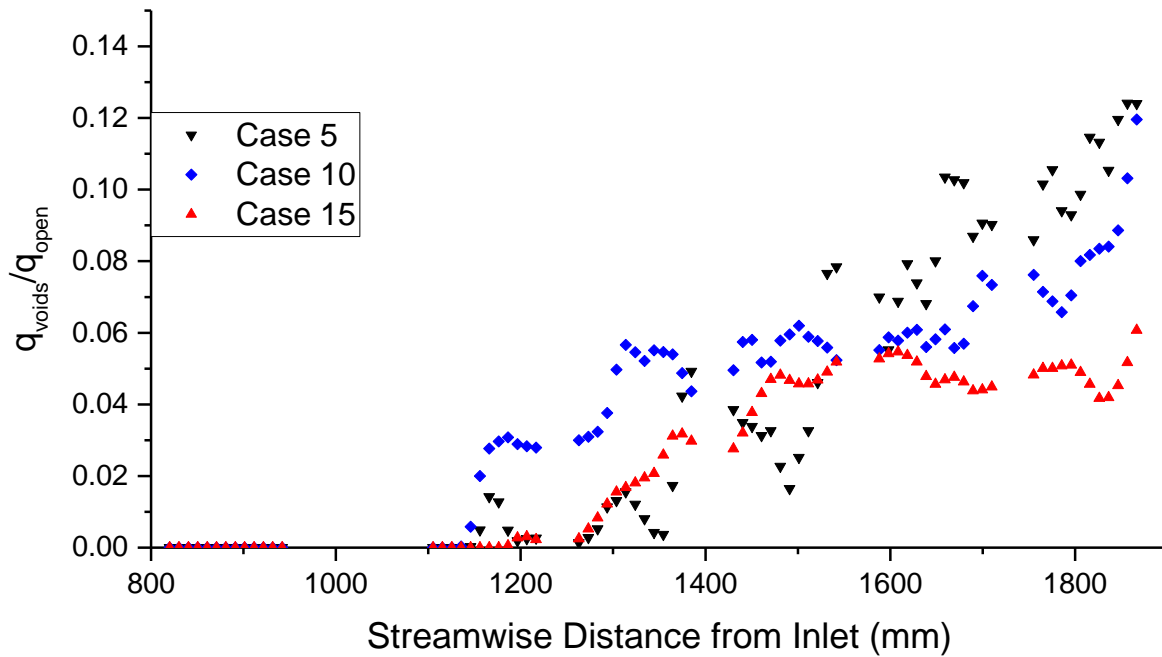


Figure 28 - Calculated seepage ratio along channel

The seepage ratio provides a much more visible representation of the changes in void flow across the length of the jam, as shown in Figure 28. The percentage of seepage flow increases along the length of the jam, in general, however does show a degree of scatter. Additionally, some areas drop to zero despite being within the jam length, namely in the 5 cm case at the most upstream end of the jam when the jam had a thickness of only one or two pellets and available flow area within the jam becomes small. In general, however, the seepage flow reaches up to between 5 and 12% of total discharge, which does show it to be a significant component of flow even in the case of a non-grounded jam. Figure 28 is not expected to show the same trends in each test case as the ice jam thickness profiles were not necessarily the same. The seepage ratios are compared with thickness ratios, $\frac{t_i}{h_{open}}$, in Figure 29 to show how seepage flow relates to the percentage of flow area obstructed by the ice jam.

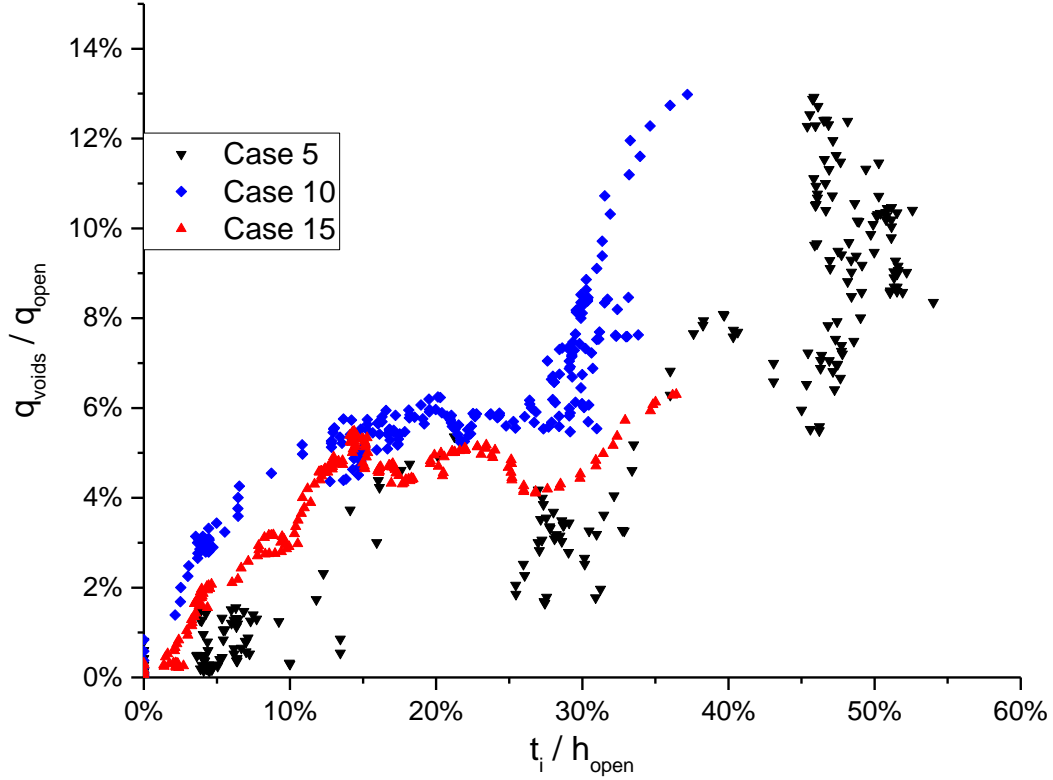


Figure 29 - Seepage ratio related to jam thickness ratio

In the 15 and 10 cm cases the data seems to follow a similar trend, with seepage increasing from zero quickly, and remaining at around 5% until the jam starts to become very thick. They also appear to follow some form of polynomial function, starting at a (0,0) intercept and accelerating upward at the highest tested thicknesses. It is possible that this trend would continue upward toward (1,1), as would represent a grounded jam, however this methodology did not achieve those extreme thicknesses. The 5 cm case is considerably more scattered and contains some gaps in the dataset such as between 15 and 25% thickness ratios. This data gap resulted from the jam not thickening at a constant rate along its length, but rather staying at a constant thickness then jumping up to a larger value quickly as was seen in Figure 14, causing the data to be more

clumped near the 5, 30, and 45% thickness ratios. It still does seem to show a similar trend, only significantly less consistent.

To fit a polynomial to the dataset, all three test cases were combined into one, providing a single equation representing the best fit of all data. Equations could be fit to each case individually with better correlation; however, the resulting three equations are fairly different, since each case had showed slightly different trends in Figure 29, with no information on which is more universally appropriate. A third order polynomial function was fitted to the amalgamated data of Figure 29, resulting in the following function, where $\frac{q_{voids}}{q_{open}}$ is the seepage ratio and $\frac{t_i}{h_{open}}$ is the jam thickness ratio:

$$\frac{q_{voids}}{q_{open}} = 2.28 \left(\frac{t_i}{h_{open}} \right)^3 - 1.83 \left(\frac{t_i}{h_{open}} \right)^2 + 0.554 \left(\frac{t_i}{h_{open}} \right) \quad 26$$

Equation 26 remains an empirical representation of the seepage behaviour in these particular test conditions and may not relate to other jams comprised of different rubble geometries or flow conditions. Of note is that the resulting equation does pass through both (0,0) and (1,1), which are the two physically-based boundaries outside the measured data, the first being open water and consequently no seepage and the second being a fully grounded jam and consequently all flow being seepage. The regression had an R^2 value of 0.74 and is shown plotted overtop of the amalgamated dataset in Figure 30. This equation does seem to follow the same trend as the datasets, but still does not have a particularly high correlation due to the scatter in initial data and because it is a best fit to all combined test cases which differed slightly from each other to begin with.

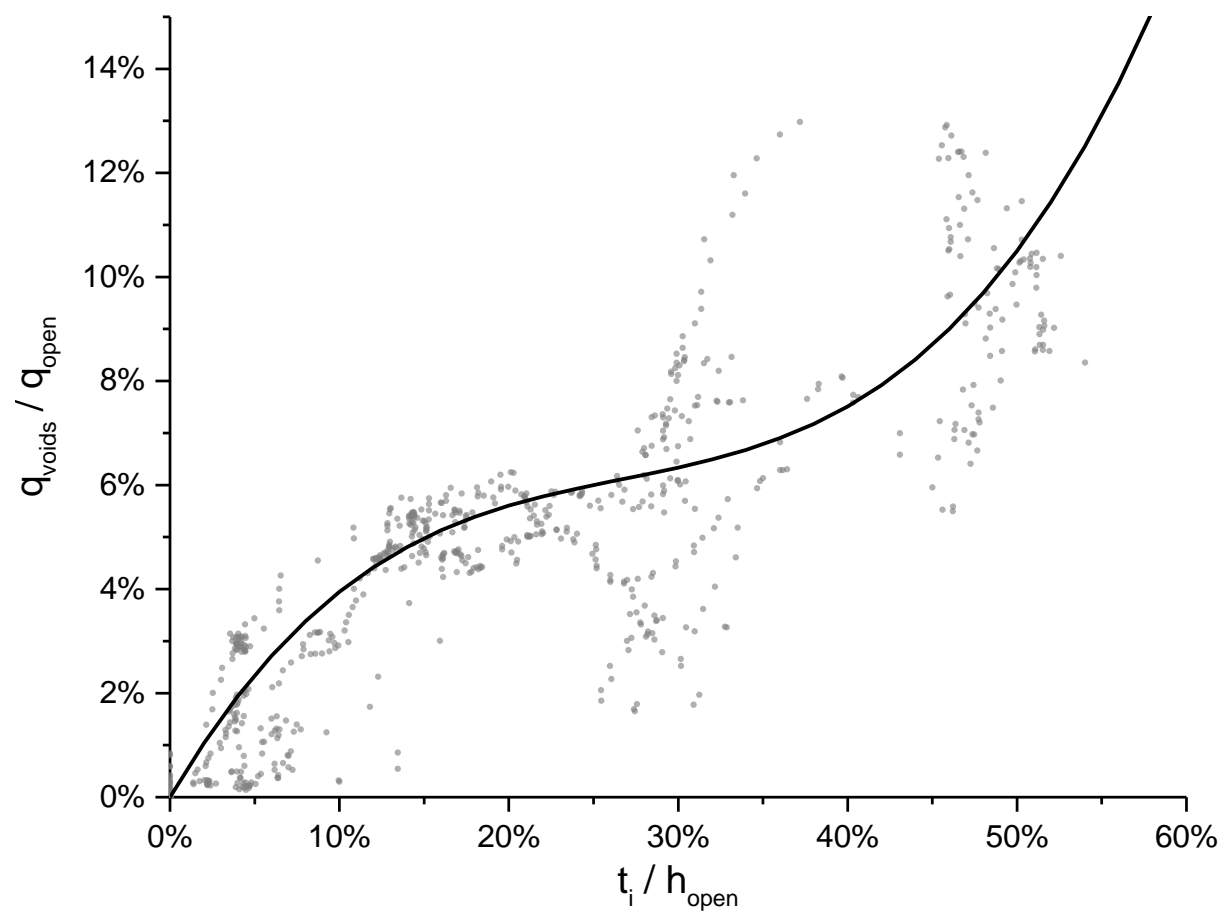


Figure 30 - Fitted polynomial relating seepage ratio to thickness ratio.

5 Discussion

5.1 Seepage

One goal of this experiment was to find a method for measuring the seepage velocity parameter (λ) without the use of a grounded jam. Based on equation 3, the values required to back-calculate seepage velocity would be seepage flowrate, Q_v , flow area within the jam, A_j , and the slope of the hydraulic gradient, S_w if it were rearranged as the following equation, where h_j is the height of the flow area within the jam, and q_v is the calculated seepage velocity from profile integration:

$$\lambda = \frac{A_j \sqrt{S_w}}{Q_v} = \frac{h_j \sqrt{S_w}}{q_v} \quad 27$$

However, in this experiment the hydraulic gradient was extremely flat along the test area. It could only be approximated using ruler measurements outside the flume, and the change in hydraulic grade line across the length of the jam was very small, even smaller than the local fluctuations caused by surface tension effects at the sidewalls of the flume. Without manometers or some other method of more accurately measuring S_w , there was no way to directly calculate λ at every location along the jam. Instead, possible values of λ were calculated for the entire jam by estimating what seepage velocities would be needed to result in the flat hydraulic gradient observed.

To solve equation 27 (or any re-arrangement of it) at least one of λ or S_w would have to be assumed. A script was developed to calculate the hydraulic grade line along the jam based off an assumed value of λ . Taking h_t as the total hydraulic head, the flow depth within the jam, h_j , can be determined by subtracting the under-ice flow depth, h , at a given location, i . The slope of

hydraulic gradient is then calculated, followed by using that slope to calculate the elevation of the hydraulic grade line at the next location, $i+1$. This process is shown in equations 28 to 30 and can be iterated along the entire length of the jam, starting from the upstream end where h_t can be assumed to be the open water depth.

$$h_{j,i} = h_{t,i} - h_i \quad 28$$

$$S_{w,i} = \left(\frac{q_{v,i}}{\lambda h_{j,i}} \right)^2 \quad 29$$

$$h_{t,i+1} = h_{t,i} - S_w \Delta x \quad 30$$

After iterating this process for the entire ice jam results in an estimation for the hydraulic gradient required to pass the calculated amount of void seepage at the assumed seepage velocity value. This procedure was performed for each of the three test cases, and repeated with different values for λ . To determine a seepage velocity value that could be considered reasonable for these jams, the above procedure was repeated until finding a hydraulic gradient which dropped less than 2 mm along the entire jam length. While 2 mm may not have been the exact actual drop in h_t as surface tension prevented accurate measurements of the HGL the real value was unknown but was very flat and likely less than this value.

The results of this procedure provided a single minimum seepage velocity of 0.57 m/s, which is much lower than the ~1.6 m/s reported by Beltaos (1999), however is closer to the values that would be calculated in a typical ice jam using equation 4, usually closer to 0.9 m/s (Beltaos, 1999). It is also reasonable that seepage velocities would be lower in this experiment due to the consistent, rounded ice geometry providing lower void sizes than would appear between large rubble blocks.

5.2 Secondary Flow

The very low aspect ratios required in this experiment were expected to result in some form of secondary flow within the channel which could affect the validity of the 2D flow assumptions used for seepage calculation. Figure 31 shows the mean velocity contours for Case 15 at the upstream plane. The leftmost plots are at the centerline (shown previously in Figure 15 and Figure 17) while the next columns show the planes offset from the center.

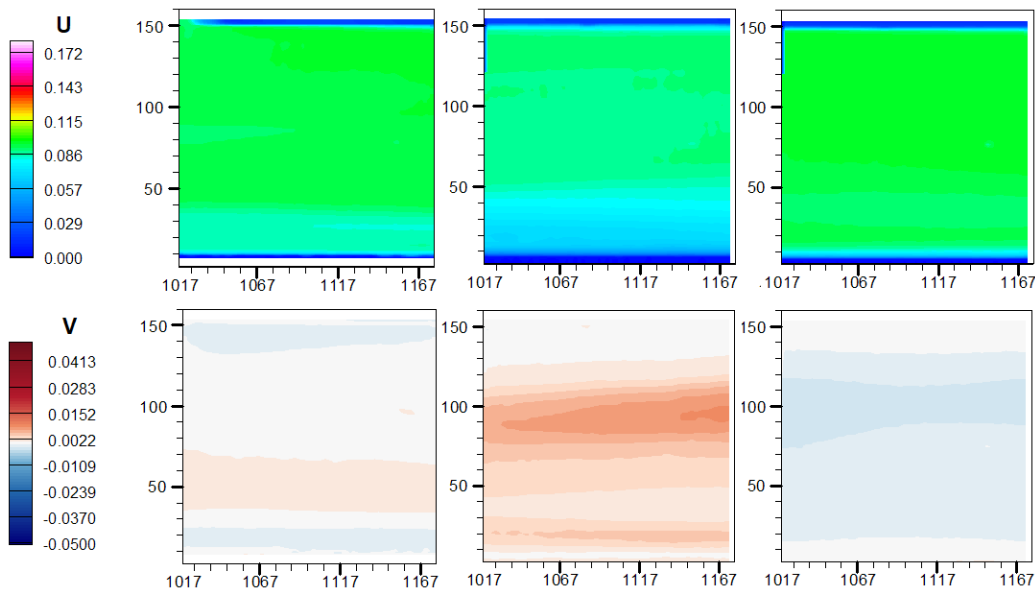


Figure 31 - Upstream mean velocity contours for Case 15 at centerline (left), offset 20 mm (middle) and 54 mm (right).

The U contours show very little change between planes, however a slight decrease in velocity does exist in the 20 mm offset plane, with a slight increase at the 54 mm offset. These are shown more clearly in the difference plots in Appendix A.4. Vertical velocity components do see fairly drastic change across the span of the channel. Upward velocities are much higher in the 20 mm offset plane, which differs from what would be expected in the case of a symmetrical, surface

diverging secondary flow that would feature the largest upward velocities in the centre. If the flow is assumed to be symmetrical, one would expect the same upward velocities on the near-side of the flume, suggesting the presence of two surface-diverging flow cells.

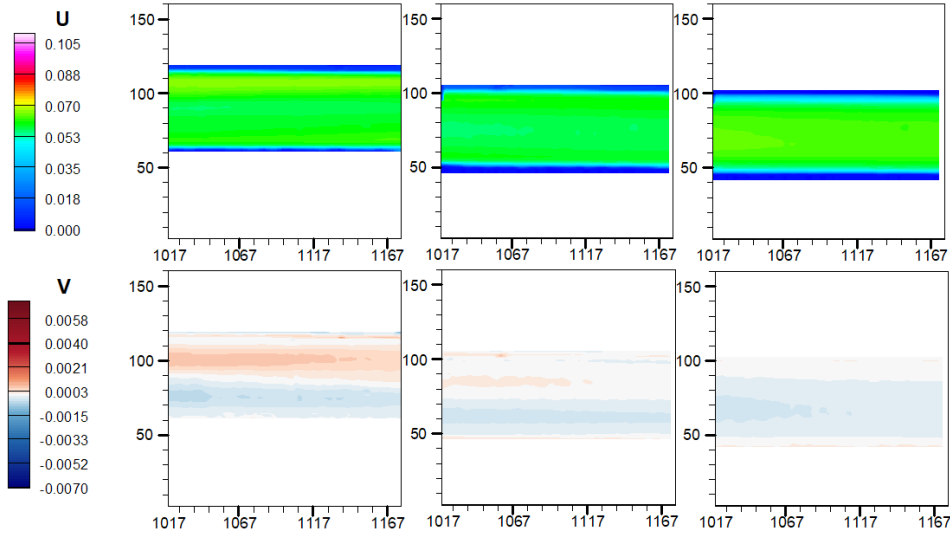


Figure 32 - Upstream mean velocity contours for Case 5 at centerline (left), offset 20 mm (middle) and 54 (right) mm.

Figure 32 shows similar contours for Case 5, however features a much more predictable result where V is positive at the centreline and decreases gradually toward the wall. The centerline plane does show downward velocities near the bed – a behaviour visible in the centerline of all three test cases – but does not appear to recirculate upward at the walls in any of the studied planes, but may do so closer at greater offsets, as these were not captured. Figure 33 summarizes the data in the contour plots with a single profile from each, for both the 15 and 5 cm test cases. These profiles emphasize the magnitude of the secondary circulation effects more clearly, in particular showing the 15 cm (low aspect ratio) case to feature much more prominent changes in flow across the span of the channel, as well as much larger vertical velocities of approximately

$0.05*U_{max}$ compared to $\sim 0.01*U_{max}$. Some of the difference in each profile may be attributed to changes in jam geometry between capture of each offset plane, as the jam had to be reconstructed after re-calibrating the field of view, and there is no way beyond simply measuring jam thickness to ensure that the upstream flow condition was exactly the same in each case.

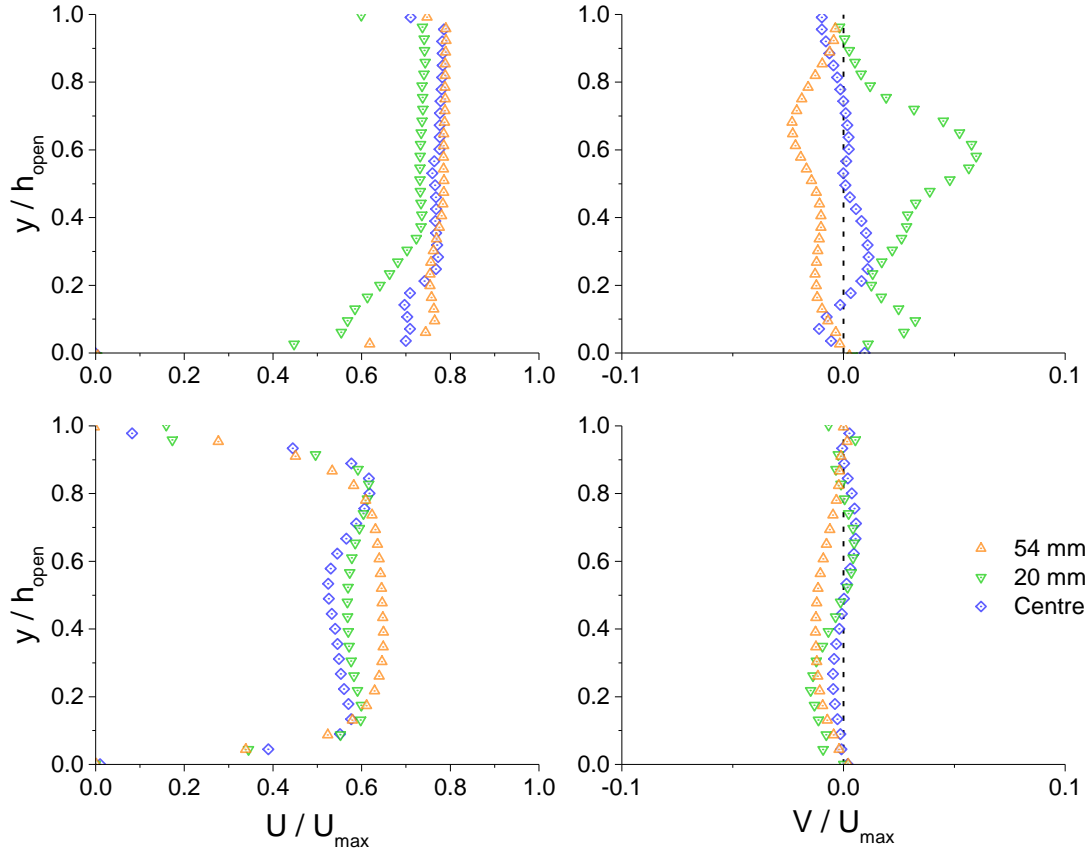


Figure 33 - Mean velocity profiles for U (left) and V (right) in Case 15 (top) and 5 (bottom).

Based on these results, it is apparent that in no cases can the flow be assumed two dimensional, although the significance of secondary flow becomes much smaller in the lowest depth test case. Figure 34 shows a visual representation of the secondary flow conditions which may be occurring within the flume to produce the results shown above. These estimations assume that

the flow is symmetrical across the centreline, which is not necessarily the case as the ice jam may not be symmetrical, however as can be seen by the locations of the laser sheets in Figure 34, no planes were taken on the other side of the flume to clarify symmetry. Collecting additional planes on the other side of center would have been possible with more time, however, wouldn't have provided much additional benefit. They would again require reconstruction of the jam each time the camera was moved, never guaranteeing that any asymmetry the jam shape may cause would be the same in the new planes.

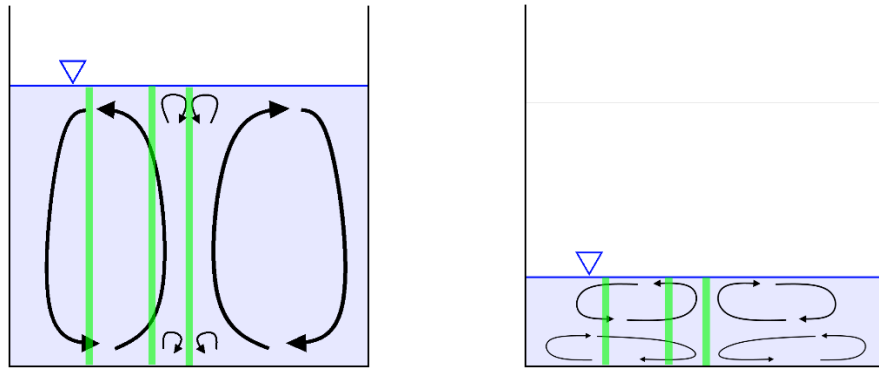


Figure 34 - Estimation of secondary flow cells in Case 15 (left) and 5 (right).

5.3 Limitations and Sources of Error

Several limitations arose during this experiment due to the novel nature of the methodology, and while most were corrected to a degree, some sources of error did remain through to the final data. These limited the quality of the final datasets, the degree of accuracy with which seepage could be calculated, as well as the ability to accurately define the seepage coefficient based on the recorded data.

One of the most apparent sources of error in the results appeared to be due to the settling of particles during testing. While the exact rate at which particles were lost is not known due to the effects of turbulence on settling velocities, it was apparent simply from inspection of the accumulating dusty layer on the channel bed that particles were settling at a significant rate during the tests. While the methodology of this test was designed to minimize the time particles were allowed to settle through cleaning the bed and reconstructing jams, the erroneous streaks visible in Figure 22 and the other turbulence contours shows that settling still had impacts, particularly on the 10 cm test case. The 5 and 15 cm tests were done approximately two weeks earlier than the 10 cm one, and the resulting cleaner water may have made these tests less sensitive to the light scattered by settled particles. Better turbulence data could have been acquired by cleaning the bed after every plane, rather than after every other plane, solving the alternating planes of erroneous turbulence data seen in Case 10. However, this creates a trade-off with the quality of calculated specific discharge, as every time the jam is rebuilt there remains the possibility of small changes between jam profiles. More reconstructions will increase the discontinuities found in calculated discharge, requiring additional corrections. Maximizing the quality of seepage calculation would require capturing the entire profile at once before any settling occurs, which could be done by reducing the number of images in each plane or by using more than one camera to capture multiple planes simultaneously. This thesis used an approach that compromised between turbulence and discharge quality but repeating the experiment with only 2000 images per plane could allow for good discharge data if no turbulence statistics are desired.

Several limitations were imposed by the facility used for this experiment, due to the size of the flume and the integrated equipment. While the small-scale flume was chosen due to being a manageable size for the first venture into this style of ice-jam research, some scaling limitations materialized due to the short length of flume, which contributed not only to the lack of fully developed flow but also required the use of manual ice jam thickening as the jam would otherwise accumulate to the entire length of the flume and leave no space for additional pellets. Larger ice pieces or ice floes were also kept out of use by the small scale, as blocks would have to be cut to extremely small dimensions to keep the block width values at acceptable percentages of the channel width. The design of the flume also prevented from placing a catch basin after the flume outfall, instead requiring the catch screen in the flume and allowing this screen to become a contributing factor to unwanted channel obstruction. Relating to the channel obstruction was the behaviour of the pump causing the flowrates to be difficult to control amongst tests. As slight changes in the amount of screen obstructed could cause the pump to change its discharge, resulting in the slight differences in calculated discharge between planes where the jam was reconstructed. Adding a flowmeter to the flume would allow the pump to be continually adjusted to maintain the exact discharge regardless of obstruction.

6 Conclusions and Future Work

A methodology was developed for analyzing flow under simulated ice jams using PIV, comparing the flow conditions of three test cases at different open water depths. Mean velocity contours showed the streamwise acceleration of flow as the jam thickened, as well as the presence of secondary flow regions under flatter sections of the jams. Turbulence statistics were calculated under each jam for streamwise and vertical turbulence intensity and Reynolds shear stress.

Integration was performed on the velocity profiles in each test case to determine values for specific discharge in the flume at each location. The values under the jam were subtracted from the open water discharges to determine the portion of flow travelling within the voids of the ice jam. This void seepage was calculated along each jam profile, relating the percentage of seepage flow to the thickness of the jam. The percentage of seepage flow was shown to increase nonlinearly when more of the channel is obstructed by the ice jam. Seepage remained most commonly around 5 to 6% of total flow at lower jam thicknesses but was observed to increase as high as 14% of total flow when the jams reached upwards of 40% of the total channel depth. While the values of seepage flow are relatively small compared to those which would occur at grounded or partially grounded jams, this data still showed seepage ratios to be large enough to remain significant even in floating jams. Based on the recorded seepage measurements, the seepage velocity was estimated to be 0.57 m/s.

6.1 Future Work

For future work, the first and most important factor to be improved is the scaling of the experiment, as the current implementation limited the length of the jam and the aspect ratio of the channel. When the model jam forms naturally (as opposed to with the manual thickening used in this experiment) the jam angle tends to be very small, thus requiring a long jam to attain any significant thickness. A longer flume could allow for these lower jam angles, as the model ice could be discharged far enough upstream to not impact the longer jams. The lack of fully developed flow could be improved upon as it would make the results more easily comparable to previous work, and a longer flume and potentially longer trip should help by leaving more open water between the inlet and the jam. Secondary flow is also problematic for this experiment as the calculation of seepage uses an assumption of 2D flow under the jam. The significance of secondary flow was shown to be greater at the lower aspect ratio (higher depth) tests, and so use of a wider channel would help to increase the aspect ratio and potentially improve on these results.

Another continuation of this experiment would be to use a different type of model ice, namely larger blocks rather than rounded pellets. While the pellets used in this experiment are a reasonable scale with respect to the channel width, the consistent shape and roundness results in generally smaller voids within the jam as well as a relatively smooth jam underside. Large, flat blocks of varied dimensions would be more typical of a realistic breakup jam, and if done correctly (requiring the aforementioned larger flume sizes) would provide a rougher, jagged jam underside with the complex flows that could more fully utilize the potential of the PIV analysis. These flows affect the behaviours of ice pieces in a jam, and the PIV system would have a

unique capability of showing the movement of water around protruding blocks of model ice at a proximity that could not be achieved by any other measurement technique.

Large blocks remain difficult to use if the rest of the experimental setup and methodology is kept identical, as these blocks were tested in the preliminary experiments for this thesis and were found to clog the entirety of the screen far too quickly to perform any analysis. Creating a similar jam using only a partial obstruction, such as a floating ice cover or partial-depth screen, would prevent any such blockage from occurring. Space constraints prevented that from being feasible in this experiment however, as this would also require continual removal of the pieces of ice that transport underneath before they obstruct the catch screen and continual addition of new ice upstream to replace them. Constructing an apparatus to maintain this condition, recycling transported ice to reintroduce upstream, would allow for a jam to be studied in a more dynamic state typical of real ice jams, and would also allow for new variables to be controlled such as the rate of ice discharge and the depth ratio of the screen itself. Even in the current experiment allowing ice transport, combined with a recycling system, would also have helped prevent the unreliable flowrates caused by the obstruction of the screen.

If a future design were to incorporate larger blocks, the more jagged and intricate jam underside would be interesting to examine for 3D flow to visualise flow diverging around protruding blocks. This could be done using tomographic 3D-3C PIV in a select area of interest, even if most of the jam was to be analyzed with similar 2D planar PIV for computational efficiency.

Lastly, the application of this work would be to ideally improve upon hydraulic models, so creating a similar system in a program such as HEC-RAS to compare the experimental results with modelled ones would be useful, especially for demonstrating the impacts of seepage.

References

- Adrian, R. J. & Westernweel, J., 2011. *Particle Image Velocimetry*. 1st ed. New York: Cambridge University Press.
- Arthur, J. K., 2012. *Flow through and over model porous media with or without inertial effects*, Winnipeg: University of Manitoba.
- Ashton, G., 1974. Froude criterion for ice block stability. *Journal of Glaciology*, 13(68), pp. 307-313.
- Ashton, G. D., 1978. River Ice. *Annual Review of Fluid Mechanics*, 101(1), pp. 369-392.
- Bear, J., 1989. *Dynamics of Fluids in Porous Media*. 2nd ed. New York: Dover Publications, Inc..
- Beltaos, S., 1988. Configuration and properties of a breakup jam. *Canadian Journal of Civil Engineering*, 15(4), pp. 685-697.
- Beltaos, S., 1995. *River Ice Jams*. Highlands Ranch(Colorado): Water Resources Publication, 1995.
- Beltaos, S., 1999. Flow through the voids of breakup ice jams. *Canadian Journal of Civil Engineering*, 26(2), pp. 177-185.
- Beltaos, S., 2001. Hydraulic Roughness of Breakup Ice Jams. *Journal of Hydraulic Engineering*, 127(8), pp. 650-656.

Beltaos, S., 2008. Progress in the study and management of river ice jams. *Cold Regions Science and Technology*, Volume 51, pp. 2-19.

Beltaos, S. & Burrell, B. C., 2006. Water temperature decay under breakup ice jams. *Cold Regions Science and Technology*, 45(3), pp. 123-136.

Beltaos, S., Miller, L., Burrell, B. & Sullivan, D., 2006. Formation of Breakup Ice Jams at Bridges. *Journal of Hydraulic Engineering*, 132(11), pp. 1229-1236.

Coleman, H. & Steele, W., 1995. Engineering application of experimental uncertainty analysis. *AIAA*, Volume 33, pp. 1888 - 1896.

Coutermarsh, B. & McGilvary, R., 1994. *Analyzing the Stability of Floating Ice Floes*, Hanover, New Hampshire: US Army Corps of Engineers, Cold Regions Research & Engineering Laboratory.

Daly, S. & Axelson, K., 1990. Stability of floating and submerged blocks. *Journal of Hydraulic Research*, 28(6), pp. 737-752.

Dow Ambtman, K. E., Hicks, F. E. & Steffler, P. M., 2011. Experimental Investigation of the Pressure Distribution beneath a Floating Ice Block. *Journal of Hydraulic Engineering*, 137(4), pp. 399-411.

Dow Ambtman, K. E., Steffler, P. M. & Hicks, F. E., 2011. Analysis of the Stability of Floating Ice Blocks. *Journal of Hydraulic Engineering*, 137(4), pp. 412-422.

Dow Ambtman, K. & Hicks, F., 2012. Field Estimates of Discharge Associated with Ice Jam Formation and Release Events. *Canadian Water Resources Journal*, 37(1), pp. 47-56.

- Eliasson, J. & Gröndal, G. O., 2008. Development of a river ice jam by a combined heat loss and hydraulic model. *Hydrology and Earth System Sciences*, Volume 12, pp. 1249-1256.
- Ettema, R., 2017. Flume Findings on the Transverse Variation of Wide-Jam Thickness in a Bend. *Journal of Cold Regions Engineering*, 31(4).
- Ettema, R. & Muste, M., 2001. Laboratory Observations of Ice Jams in Channel Confluences. *Journal of Cold Regions Engineering*, 15(1), pp. 34-58.
- Gogus, M. & Tatinclaux, J.-C., 1981. Mean characteristics of asymmetric flows: application to flow below ice jams. *Canadian Journal of Civil Engineering*, Volume 8, pp. 342-350.
- Healy, D. & Hicks, F. E., 2006. Experimental Study of Ice Jam Formation Dynamics. *Journal of Cold Regions Engineering*, 20(4), pp. 117-139.
- Healy, D. & Hicks, F. E., 2007. Experimental Study of Ice Jam Thickening under Dynamic Flow Conditions. *Journal of Cold Regions Engineering*, 21(3), pp. 72-91.
- Kennedy, R. J., 1958. Forces Involved in Pulpwood Holding Grounds - I. Transverse Holding Grounds with Piers. *The Engineering Journal*, Volume 41, pp. 58-68.
- Lowe, S. A., 2003. Omission of Critical Reynolds Number for Open Channel Flows in Many Textbooks. *Journal of Professional Issues in Engineering Education and Practice*, 129(1), pp. 58-59.
- Murray, A., Essel, E. & Dow, K., 2019. *Laboratory Investigation of Void Seepage and Flow under Simulated Ice Jams*. Ottawa, Committee on River Ice Processes and the Environment.

- Nakagawa, H., Nezu, I. & Ueda, H., 1975. Turbulence of open channel flow over smooth and rough beds.. *Proceedings of Japan Society of Civil Engineers*, Volume 241, pp. 155-168.
- Nezhikhovskiy, R., 1964. Coefficients of roughness of bottom surface on slush-ice cover. In: *Soviet Hydrology*. Washington: American Geophysical Union, pp. 127-150.
- Nezu, I. & Nakagawa, H., 1993. *Turbulence in Open-Channel Flows*. Rotterdam, Netherlands: A.A. Balkema.
- Nyantekyi-Kwakye, B. et al., 2018. Roughness effect on turbulent flow structure beneath a simulated ice jam. *Journal of Hydraulic Research*.
- Pahlavan, H., 2016. *An Experimental Investigation of Turbulent Flow Characteristics Beneath a Simulated Ice Jam*, Winnipeg, MB: University of Manitoba.
- Pariset, E. & Hausser, R., 1961. Formation and evolution of ice covers on rivers. *Transactions of the Engineering Institute of Canada*, 5(1), pp. 41-49.
- Pariset, E., Hausser, R. & Gagnon, A., 1966. Formation of ice covers and ice jams in rivers. *ASCE Journal of the Hydraulics Division*, Volume 92, pp. 1-24.
- Peters, M. et al., 2017. Experimental investigation of the flow characteristics beneath partial ice covers. *Cold Regions Science and Technology*, Volume 142, pp. 69-78.
- Prowse, T. D., 1990. Heat and mass balance of an ablating ice jam. *Canadian Journal of Civil Engineering*, Volume 17, pp. 629-635.
- Raffel, M., Willert, C. E. & Kompenhans, J., 1998. *Particle Image Velocimetry: A Practical Guide*. 3 ed. Berlin: Springer.

- Tatinclaux, J.-C. & Lee, C.-L., 1978. Initiation of ice jams - a laboratory study. *Canadian Journal of Civil Engineering*, 5(2), pp. 202-212.
- Teal, M. J., Ettema, R. & Walker, J. F., 1994. Estimation of Mean Flow Velocity in Ice-Covered Channels. *Journal of Hydraulic Engineering*, 120(12), pp. 1385-1400.
- Urroz, G. E. & Ettema, R., 1992. Bend ice jams; laboratory observations. *Canadian Journal of Civil Engineering*, Volume 19, pp. 855-864.
- Uzuner, M. & Kennedy, J., 1972. Stability of floating ice blocks. *Journal of the Hydraulics Division*, Volume 98, pp. 2117-2133.
- Wang, J. et al., 2016. The impact of bridge pier on ice jam evolution - an experimental study. *Journal of Hydrology and Hydromechanics*, pp. 75-82.
- Wang, J., Sui, J.-y., Chen, P.-p. & Hirshfield, F., 2012. Mechanisms of ice accumulation in a river bend - an experimental study. *International Journal of Sediment Research*, 27(4), pp. 521-537.
- White, K. D., 1991. *Determining the Intrinsic Permeability of Frazil Ice*, s.l.: Cold Regions Research & Engineering Laboratory (U.S.); Engineer Research and Development Center (U.S.).
- White, K. D., 2003. Review of prediction methods for breakup ice jams. *Canadian Journal of Civil Engineering*, 30(1), pp. 89-100.
- Wong, J., Beltaos, S. & Krishnappan, B. G., 1985. Laboratory tests on surges created by ice jam releases. *Canadian Journal of Civil Engineering*, 12(4), pp. 930-933.

Wong, J., Beltaos, S. & Krishnappan, B. G., 1985. Seepage flow through simulated grounded ice jam. *Canadian Journal of Civil Engineering*, 12(4), pp. 926-929.

Ye, Q., Schrijer, F. F. & Scarano, F., 2016. Geometry effect of isolated roughness on boundary layer transition investigated by tomographic PIV. *International Journal of Heat and Fluid Flow*, Volume 61, pp. 31-44.

Zhang, C., Vasilevskis, S. & Kozlowski, B., 2018. *Particle Image Velocimetry: User Guide*, Aalborg, Denmark: Aalborg University: Department of Civil Engineering.

Zhao, X., Lian, J.-j. & Song, X.-y., 2017. Analyses of the stability of submerged ice blocks. *Journal of Hydrodynamics*, 12 March, 29(3), pp. 460-469.

Zufelt, J. E. & Ettema, R., 1997. *Unsteady Ice Jam Processes*, s.l.: Cold Regions Research and Engineering Laboratory.

Appendices

A.1 Convergence Test

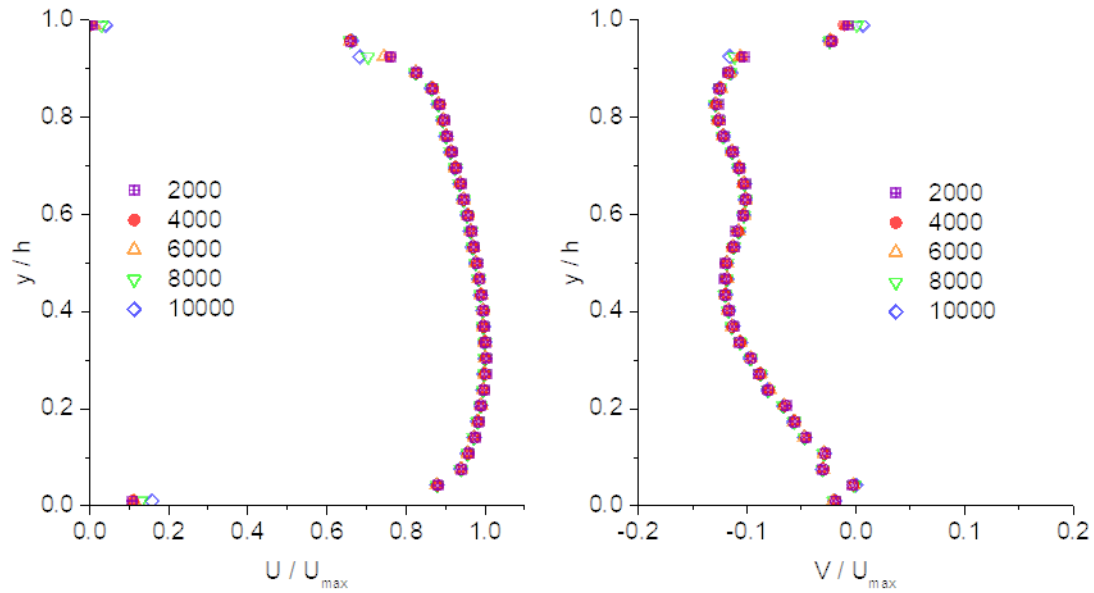


Figure 35 – Convergence for first order mean velocity statistics.

A convergence test was performed on an open water test at the upstream-most plane (Plane 1) prior to collecting the bulk of test data. 10 000 images were captured and analyzed in parts of 2000, 4000, 6000, 8000, and the full 10 000. In all convergence plots the chosen 8000 image set is displayed as the filled data points.

The first result above shows the convergence of the mean velocity profiles, and it is fairly clear that the results had converged even by the 2000th image. In a hypothetical experiment only concerned with seepage calculations and no turbulence statistics, it would therefore be unnecessary to take as many images as were taken in this experiment.

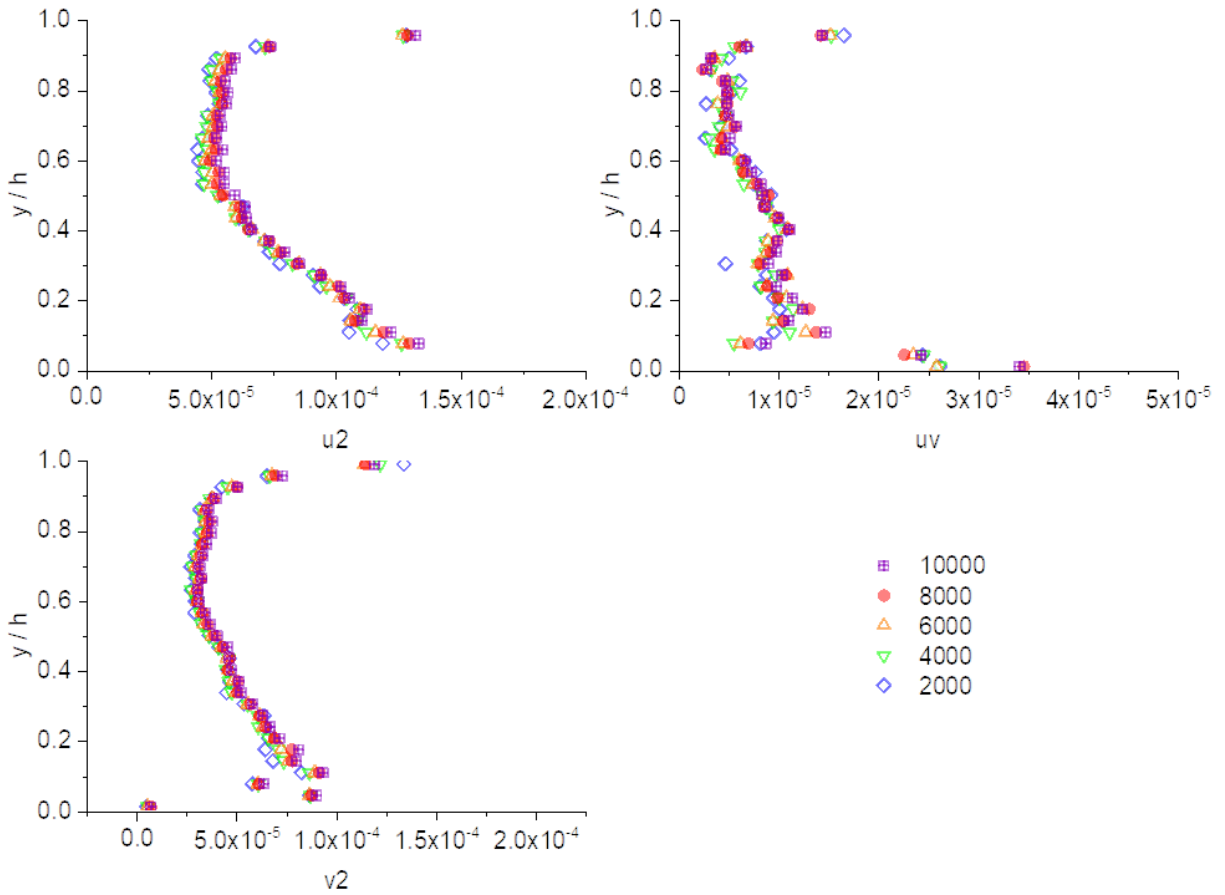


Figure 36 – Convergence results for second order turbulence statistics.

Above shows the convergence results for the first order turbulence statistics, with the streamwise and wall-normal Reynolds stresses u^2 and v^2 and Reynolds Shear uv . It is clear that the u^2 and v^2 converged relatively quickly, with only slight differences between the data sets, and the chosen 8000 image set being very close to the largest set.

The Reynolds Shear was more scattered at lower image counts, and never became particularly smooth even at larger counts, however the 8000 and 10 000 image sets still sat relatively close at most data points.

The 8000-image set was therefore deemed to be an appropriate balance between time-intensiveness and turbulence data quality. It is also of note that the convergence test was performed before the spatial resolution test and was using a rule-of-thumb interrogation area of 32×32 , which is shown in Section A.2 to provide slightly more scattered results than the area chosen for the experimental analysis.

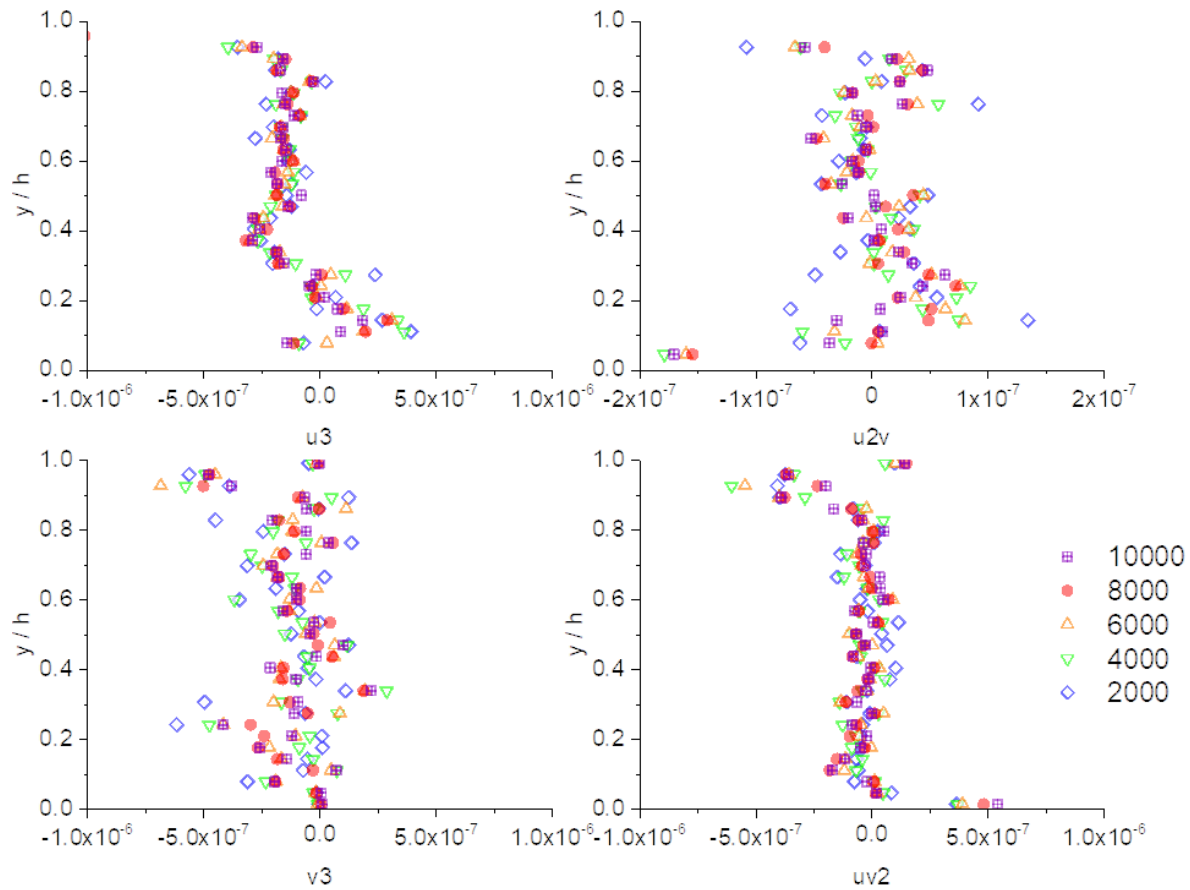


Figure 37 – Convergence results for third order turbulence statistics.

Figure 37 shows the convergence results for some third order turbulence statistics. None of these were examined in this thesis as it is clear by the scattered data that none converged even after the largest capture size of 10 000 images.

A.2 Spatial Resolution Test

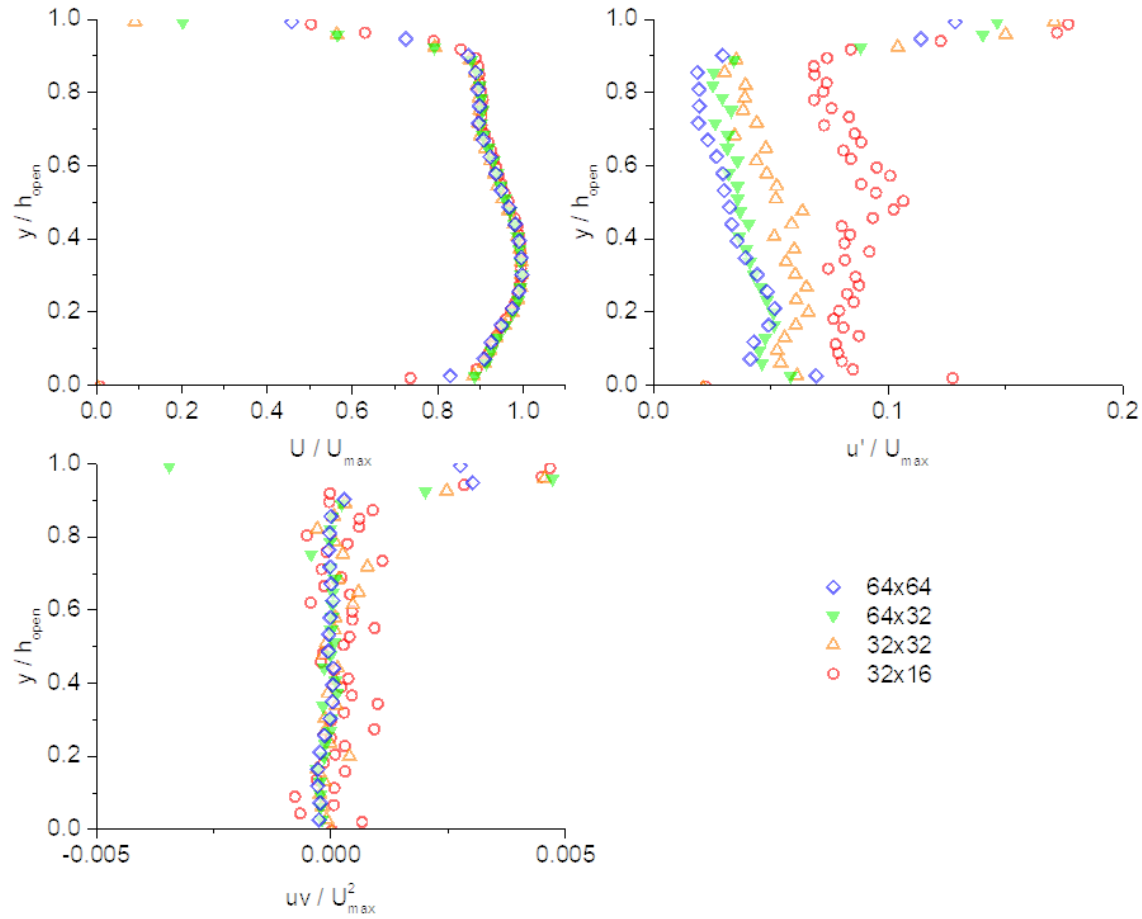


Figure 38 – Spatial resolution test results.

From the spatial resolution results in Figure 38, it is clear that the larger interrogation areas provided more consistent results for both the turbulence statistics displayed, with the 64x64 area providing the smoothest and most reasonable curves. The 64x32 results matched somewhat closely in both u' and uv with some scatter, however the 32x32 and 32x16 areas were increasingly unreliable.

Despite the 64x64 area providing the cleanest results, the analysis was performed on the 64x32 timescale to increase the number of vectors acquired in each profile as they would be needed for integration of the seepage calculations. Figure 38 also shows the mean flow statistics to be practically identical in all spatial resolutions, so the chosen 64x32 interrogation area height would still provide good U values for integration, while maintaining close to the same quality of turbulence data as the largest size.

A.3 Jam Profile Image Processing

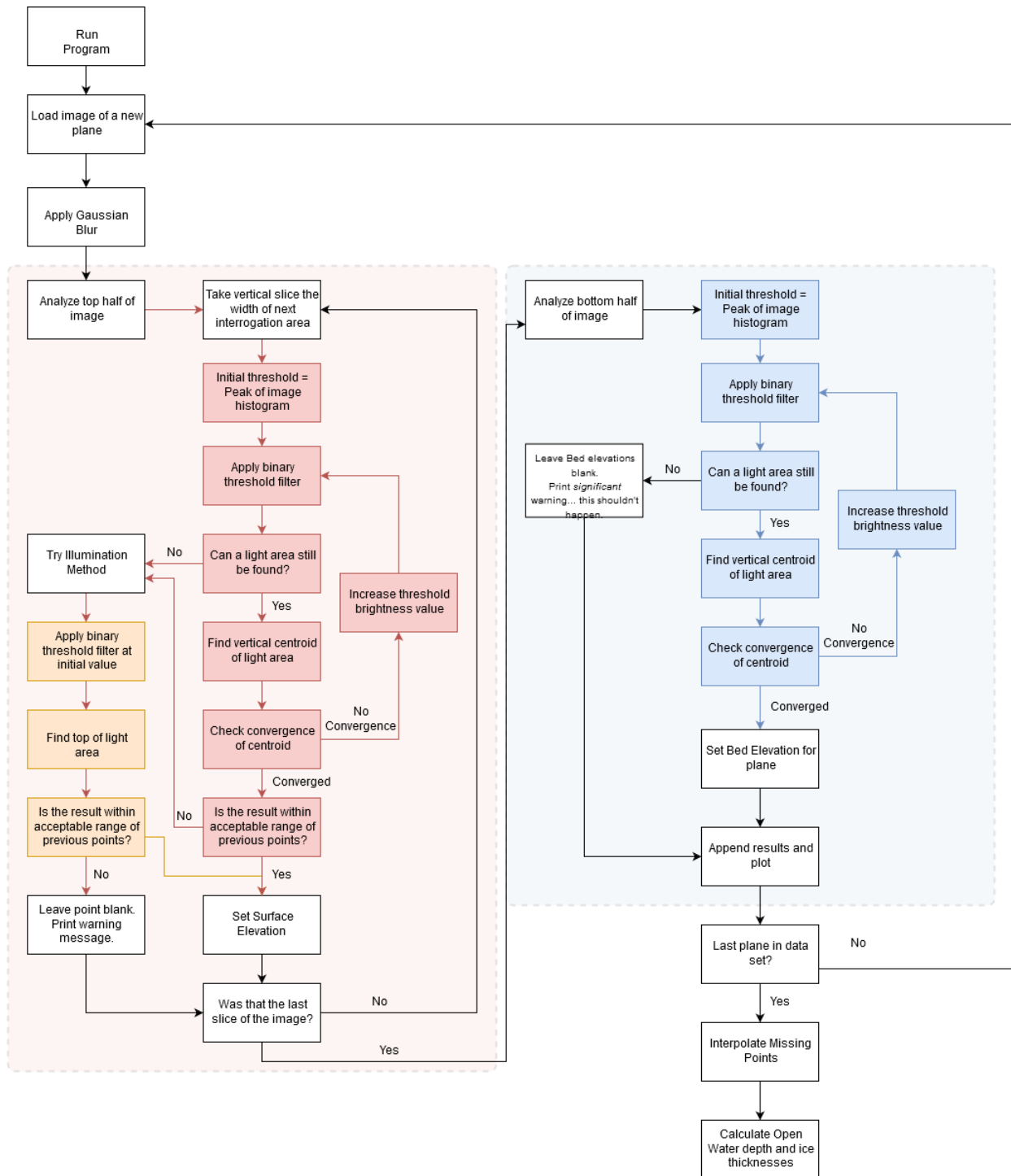


Figure 39 – Workflow diagram for image processing code.

The above workflow diagram shows the procedures used for determining the locations of the channel bed and ice jam bottom from PIV images. The red highlighted section represents the estimation of the top elevation, being either the water surface or underside of the jam, and the blue section shows the estimation of the bed elevation. The two processes are very similar with only slight differences due to greater difficulty finding the uneven jam underside compared to the perfectly flat channel bed.

A.4 Secondary Flow

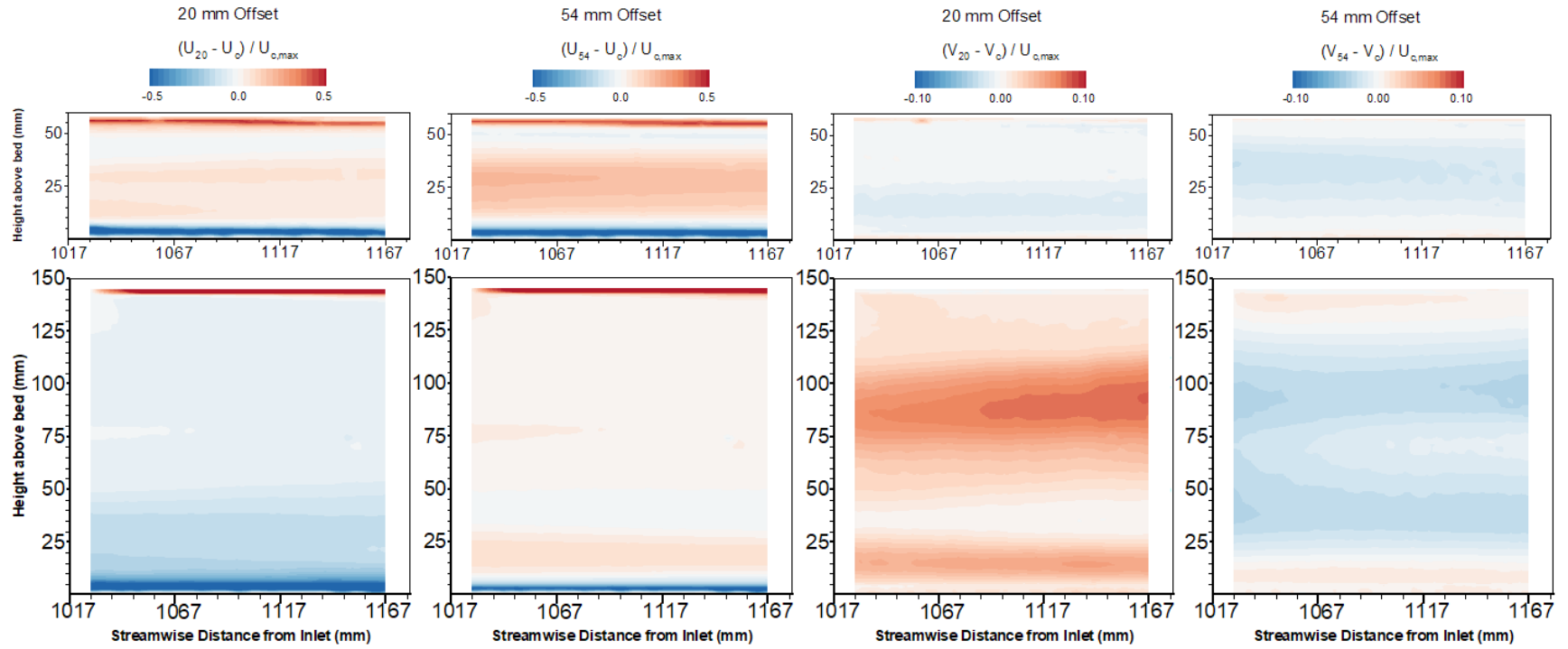


Figure 40 - Difference plots for U (left) and V (right) for off-centre planes, normalized by U_{max} for Case 5 (top) and 15 (bottom).

Figure 40 shows difference plots for the off-centre planes, normalized by U_{max} . These are calculated by subtracting the centerline velocities from those of each off-centre plane to show the change in velocity contours between them, rather than the actual values used in Figure 31 and Figure 32. Like all previous contours featuring positive and negative values, blue areas correspond to negative values (where the offset plane has a lower or more downward velocity than the centerline) and red areas correspond to positive values (where the offset plane has a higher or more upward velocity).

The 4 plots on the left-hand side show the change in streamwise velocity, and make visible the small changes in otherwise large values of U . It is clear in both cases that there is a slight increase in streamwise velocity at the 54 mm offset, with the 20 mm offset showing less increase in the 5 cm case and a slight decrease in the 10 cm case. Most of these changes remain low, however, being on the order of 10% U_{max} at their highest, and near zero in most locations.

The remaining plots on the right-hand side show the change in V in the offset planes with respect to the centerline, again normalized by U_{max} to be consistent with the previous V normalization as in Figure 18. Changes in V were already more clearly visible in the contours from Section 5.2. Figure 40 does help to reinforce the reductions in secondary flow effects at the higher aspect ratio case (Case 5) where the changes in V are very small in both the offset planes, while the values of V change quite low aspect ratio of Case 15. For Case 15, however, the difference plots end up looking very similar to the original contours in Figure 31 as the actual values of V at the centerline were already very close to 0 in most locations.

A.5 Uncertainty Analysis

Uncertainty in PIV work is estimated by combining both a *bias* and *precision error* present in the computation of velocities from image pairs. Velocities in PIV are computed using the following equation:

$$U_i = \frac{\Delta s_i L_O}{\Delta t L_I} \quad 31$$

where U_i is the component of velocity in the measurement plane (m/s), Δs_i is the displacement of the particles within the image plane in pixels, L_O is the width of the field of view of the camera (m), L_I is the width of the camera's resolution in pixels, and Δt is the pulse timing of the image pairs. Solving this equation for each velocity component provides an instantaneous velocity vector. As such, the uncertainties present in any of the four variables in the expression will contribute to the total uncertainty for a velocity measurement.

The bias errors can be estimated with the following equation (Coleman & Steele, 1995):

$$B_{Ui} = \sqrt{(\theta_{\Delta s_i} B_{\Delta s_i})^2 + (\theta_{L_O} B_{L_O})^2 + (\theta_{\Delta t} B_{\Delta t})^2 + (\theta_{L_I} B_{L_I})^2} \quad 32$$

where B_x are the bias limits for variable x as estimated based on the measurement device and θ_x is the sensitivity coefficient of the variable, calculated as the partial derivative of equation 31 by the variable x :

$$\theta_x = \frac{\partial U_i}{\partial x} \quad 33$$

The bias error was calculated for the U and V components using under-ice velocities of Case 15. Values for the bias limits for Δs and Δt are based on manufacturer's specifications. Bias limits

for the camera field of view is 0.5 mm based on the measurement device used for calibration, and the bias limit for the resolution bias is ½ of a pixel. Results of the bias error calculations are summarized in the following table.

Table 5 – Bias limits for streamwise and vertical mean velocities U and V.

Variable	Magnitude	B _x	θ _x	B _x θ _x	B _x θ _x ²
<i>Lo</i>	1.62E-01	5.00E-04	1.05E+00	5.24E-04	2.74E-07
<i>Li</i>	2.05E+03	5.00E-01	-8.30E-05	-4.15E-05	1.72E-09
<i>dT</i>	5.66E-03	1.00E-07	-3.00E+01	-3.00E-06	9.02E-12
<i>dS</i>	1.21E+01	1.27E-02	1.40E-02	1.78E-04	3.16E-08
<i>U</i>	1.70E-01			Sum Sq	3.08E-07
				Bias Error	5.55E-04
				% Bias	0.33%
Variable	Magnitude	B _x	θ _x	B _x θ _x	B _x θ _x ²
<i>Lo</i>	1.62E-01	5.00E-04	2.46E-01	1.23E-04	1.52E-08
<i>Li</i>	2.05E+03	5.00E-01	-1.95E-05	-9.77E-06	9.54E-11
<i>dT</i>	5.66E-03	1.00E-07	-7.07E+00	-7.07E-07	4.99E-13
<i>dS</i>	2.86E+00	1.27E-02	1.40E-02	1.78E-04	3.16E-08
<i>V</i>	4.00E-02			SumSq	4.69E-08
				Bias Error	2.17E-04
				% Bias	0.54%

The precision error creates scatter in a set of velocity vectors, and is created by effects such as peak locking, where the positions of small particles will tend toward integer pixel values within the image. Precision error is calculated by the following equation:

$$P_x = \frac{K\sigma}{\sqrt{N}} \quad 34$$

where P_x is the precision error of variable x , K is the confidence interval, σ is the standard deviation of the dataset of variable x , and N is the number of data points. This value was calculated for both U and V . Standard deviations were taken at 5 under-ice locations for the 8000

image dataset, and the mean of these was taken as each value of σ . The results of this process are shown in the following table.

Table 6 – Precision error for streamwise and vertical velocities, U and V .

Variable	σ_x	K	P_x
U	0.0048	2	0.01%
V	0.003	2	0.01%
N	8000		

As increases in the number of images captured tends to decrease precision error according to equation 34, the large image set used in this work results in a precision error that is insignificant compared to that of bias error. The total uncertainty is the root sum of squares of the bias and precision errors. This results in an estimated error of $\pm 0.4\%$ for U and $\pm 0.6\%$ for V .

A.6 Model Ice Properties

The density of the polyethylene pellets was measured after painting, as it was expected that applying a significant amount of oil-based paint could alter the specific gravity of the particles. Multiple cans of spray paint were applied to the pellets to get them to a dark enough colour, and as such this could significantly alter the weight of the sample. Density was measured by taking a series of samples of the painted pellets at different volumes and weighing them. The volume of void space was accounted for and the specific gravity for each test was measured. The data is summarized in the following table.

Table 7 - Model ice density measurements.

Data		Calculations		
Bulk Volume (L)	Weight (kg)	Actual V (L)	Density (kg/m ³)	SG
1.00	0.6	0.67	900	0.90
2.00	1.1	1.33	825	0.83
3.00	1.7	2.00	850	0.85
4.00	2.2	2.67	825	0.83
5.00	2.8	3.33	840	0.84
5.45	3.1	3.63	853	0.85

The average value for the specific gravity was 0.85, which is substantially lower than the estimated value for the unpainted pellets at 0.93. Changing density would have an impact on how the model ice would react to flow and to what degree it could mechanically thicken under a certain flow condition, however since the ice jams in this experiment were thickened manually this was considered to have no effect on their suitability. The lighter ice material just means the jams had a larger portion floating above the water, but no seepage flow would exist in this area anyway.